



**LUND**  
UNIVERSITY

Master thesis

## Development of a new dosimetry technique

Division of Combustion Physics

by

**Timo Tsharntke**

Supervisors: Elias Kristensson

Edouard Berrocal

Lund, June 26, 2015



**Abstract:** In order to minimize the damage inflicted in healthy tissue during radiotherapy, it is vital to verify the dose absorbed by the patient. A common approach is the use of dosimetry gels in which local radiolysis processes are induced through radiation. As the subsequent read-out using Magnetic Resonance Imaging techniques is time-consuming, the here presented thesis investigates a new approach based on light scattering to determine the absorbed dose. More precisely, a laser sheet with sinusoidal intensity modulation is employed to scan the dosimetry gel slice-wise and scattered light is detected at a  $90^\circ$ -angle which allows the determination of the local extinction coefficient  $\bar{\mu}_e$  in the sample. The idea is to relate the local extinction coefficient to the absorbed dose. In order to achieve this task, a setup for the data acquisition is built and the algorithm necessary for the calculation is written. Based upon first measurements investigating the applicability of the new approach, one can state that the new technique is of great potential as it allows the visualization of the irradiation structures with high resolution.

**Keywords:** radiotherapy, dosimetry gel, extinction coefficient, light scattering, structured illumination, laser sheet, SLIPI



# Popular Description

Radiotherapy is a common technique employed when treating cancer patients. However, the radiation can also potentially inflict great damage in the healthy tissue surrounding the tumor. Consequently, it is of great importance to verify that the radiation received by the patient is absorbed in the intended location and has the right dose. In order to implement such a so called dosimetric verification, a gelatine probe that behaves similar to human tissue when irradiated is produced. More importantly, the irradiation induces a change of structure in the gelatine sample which allows one to draw conclusions concerning the absorbed dose. Currently, the most common approach to determine the absorbed dose from structural changes in the gelatine is to use Magnetic Resonance Imaging which is the same technique used to image tiny fractures in bones or to do brain scans. However, this technique also has a few disadvantages such as high costs associated with it as well as its time-consuming nature. Therefore, this thesis investigates a new approach to draw conclusions concerning the absorbed radiation dose from structural changes in the gelatine sample.

In this new technique, a blue laser beam is first compressed into a very thin sheet which is subsequently sent into the gelatine. The particles in the gelatine scatter light into all directions and a camera detects the amount of light that is scattered at a  $90^\circ$  angle. The brighter the image of the sample in a specific point, the more light has been scattered in that specific point. Most importantly, different structures in the sample scatter the light by different amounts. The laser sheet is then moved in steps through the gelatine, thereby scanning the whole sample. At each step, the camera acquires a new image which is employed to calculate a physical quantity called extinction coefficient for each point of the sample. The extinction coefficient describes how likely light is to be scattered when passing through a specific point in the sample. Thus, the value of this extinction coefficient depends on the structure of the sample and thereby also on the absorbed radiation dose. The work presented here aims to investigate the applicability of the new technique.

The result of this thesis work is a complete setup to acquire the data as well as the algorithm necessary to calculate the extinction coefficient in each point of the sample. Based on the results, one can state that the new technique is of great potential. Not only does it allow one to image the irradiated structures in the gelatine with a very high precision, it also shortens the time necessary for data acquisition as compared to other currently employed techniques.



# Contents

<b>Abstract</b>	<b>I</b>
<b>Popular Description</b>	<b>III</b>
<b>Contents</b>	<b>V</b>
<b>Acronyms</b>	<b>VII</b>
<b>1 Introduction</b>	<b>1</b>
1.1 Outline of the Thesis . . . . .	2
<b>2 Theory</b>	<b>3</b>
2.1 Light Scattering . . . . .	3
2.1.1 Elastic Scattering . . . . .	3
2.2 Light Absorption and Emission . . . . .	5
2.2.1 Fluorescence . . . . .	5
2.3 Light extinction . . . . .	6
2.3.1 Laser extinction . . . . .	7
2.3.2 Signal attenuation . . . . .	8
2.4 Turbidity . . . . .	8
2.4.1 Optical Depth . . . . .	9
2.4.2 Scattering Order . . . . .	9
2.5 Multiply Scattered Light . . . . .	9
<b>3 Dosimetric Procedure and Considerations</b>	<b>11</b>
3.1 Gel Dosimeter . . . . .	11
3.2 Dosimetric Requirements . . . . .	12
<b>4 Structured Laser Illumination Planar Imaging</b>	<b>13</b>
4.1 Experimental Setup . . . . .	13
4.2 Extraction of the SLIPI image . . . . .	15
<b>5 Extraction of Local Extinction Coefficient</b>	<b>19</b>
5.1 Experimental procedure . . . . .	19
5.2 Calculating the extinction coefficient . . . . .	21

<b>6</b>	<b>Results and Discussion</b>	<b>25</b>
6.1	Synthetic datasets . . . . .	26
6.2	Potential error sources . . . . .	27
6.2.1	Laser fluctuations . . . . .	27
6.2.2	Depth of Field . . . . .	28
6.2.3	Reflections . . . . .	31
6.2.4	Vignetting . . . . .	38
6.3	Verification of results . . . . .	39
6.4	Probing of different dosimetry gels . . . . .	40
6.4.1	Dosimetry Gel with Pillar Structure . . . . .	40
6.4.2	Probing of spatially overlapping structures . . . . .	43
6.5	Limitations . . . . .	45
6.5.1	Scattering Particle Size . . . . .	45
6.5.2	Limit in Optical Depth . . . . .	46
<b>7</b>	<b>Summary and Outlook</b>	<b>49</b>
<b>8</b>	<b>Bibliography</b>	<b>53</b>
	<b>Acknowledgments</b>	<b>55</b>

# Acronyms

<b>CCD</b>	Charge-Coupled Device
<b>DOF</b>	Depth Of Field
<b>FWHM</b>	Full Width at Half Maximum
<b>MRI</b>	Magnetic Resonance Imaging
<b>OD</b>	Optical Depth
<b>PLI</b>	Planar Laser Imaging
<b>SLIPI</b>	Structured Laser Illumination Planar Imaging
<b>S/N</b>	Signal-to-Noise ratio



# 1 Introduction

According to the *World Cancer Report 2014* [1], the annual number of diagnosed cancers is estimated to increase by almost 70% within the next two decades, reaching an all-time high of 22 million cases. With survival rates varying significantly for different kinds of cancer and for different regions in the world, the development of new and effective treatment methods is crucial and comprises various fields of today's research. One key technology in the treatment of cancer is radiotherapy which about 40% of all cancer patients receive as part of their treatment [2]. Despite the usefulness of radiation treatment, enhancement of the existing technologies is instrumental in order to increase cancer survival rates and limit unnecessary side effects. Therefore, the thesis presented here investigates a new approach to verify the radiation dose absorbed by the patient.

Ideally, the dosimetric verification of the absorbed dose should be conducted in three dimensions as many of the advanced radiation techniques involve non-stationary beams, narrow fields or sharp dose gradients [3]. Further desired characteristics of the dosimetric procedure are a high spatial resolution (preferably even time-resolved), patient-like behavior of the system and an adequate speed. One current approach that lives up to these requirements is *3D Polymer Gel Dosimetry* which is based on a gel made out of water, radiation-sensitive monomers and a gel matrix. Upon irradiation, the monomers start binding chemically to form polymers. Moreover, the gel matrix in which the polymers are embedded conserves the spatial distribution of the polymers and thus, allows a subsequent analysis of the exposure. According to [4], *Magnetic Resonance Imaging* (MRI) is a frequent approach to read-out the desired information with high spatial resolution from the exposed gel. However, disadvantages of using MRI-based read-out techniques are their complex as well as time-consuming character and the high costs associated with the use of MRIs. Consequently, a technique that allows a faster read-out at lesser cost is highly desirable.

Therefore, this thesis focuses on a new approach to conduct the read-out by using a technique called *Structured Laser Illumination Planar Imaging* (SLIPI) which was originally developed for spray diagnostics and is based on the detection of visible laser light scattered by the sample [5, 6]. In contrast to most other light-employing read-out techniques, the SLIPI approach has the advantage of successfully removing the signal contribution from light that has been scattered more than once which would otherwise limit the accuracy of measurements. The idea is to employ a two-dimensional laser sheet to which a sinusoidal

intensity pattern is added along its height. While light experiencing multiple scattering events will lose this modulation information, photons that have only been scattered once retain the information, thus making it possible to separate their signal contribution in the data post-processing. More importantly, it has been shown that by moving the laser sheet through the sample, i.e. scanning the sample slice-wise, the local *extinction coefficient* can be extracted which describes the likelihood of a photon-matter interaction in each point of the sample [7].

The principal objective of the work presented here is to determine the local extinction coefficients in the dosimetry gels and to establish a relation to the radiation dose absorbed. In order to accomplish this objective, a SLIPI setup is built and the algorithm for the extraction of the extinction coefficient is written. Moreover, first measurements investigating the applicability and accuracy of the new approach are implemented and different methods of visualizing the irradiated structures are explored.

### 1.1 Outline of the Thesis

This thesis is structured as follows:

**Chapter 2** provides the theoretical background necessary to follow this thesis with a focus on light-matter interactions. Additionally, relevant terms are introduced and error sources are described.

**Chapter 3** gives a more detailed overview of the requirements that the dosimetry approach investigated here has to fulfill. A more thorough description of the gel samples and their production is also included.

**Chapter 4** explains the *Structured Laser Illumination Planar Imaging* technique and presents the experimental setup designed as part of this thesis.

**Chapter 5** focuses on the experimental procedure as well as the algorithm written to extract the *local extinction coefficient*.

**Chapter 6** demonstrates a quantitative as well as qualitative verification of the results as well as the steps taken to achieve these results. Moreover, it presents measurements on different dosimetry gels and investigates the applicability of the new approach for dosimetric purposes.

**Chapter 7** includes a brief summary of the work presented in chapters 4 to 6 and gives an outlook of what future directions one may investigate in this field.

## 2 Theory

In this chapter, the underlying theory is described with a focus on the interaction of light in the visible spectrum with matter. More precisely, relevant effects and terms for this thesis such as *elastic scattering* or the *extinction coefficient* are described more thoroughly.

The chapter starts out by first explaining the concepts of *light scattering* and *light absorption* before illustrating their importance for this thesis when describing *laser extinction* as well as *signal attenuation*. Lastly, the influence of *multiply scattered light* on the measurements is explained.

### 2.1 Light Scattering

In order to illustrate the concept of light scattering, one can think of a light ray which is deflected from its originally straight path by the atoms or molecules in the propagation medium. The probability per unit length for such a scattering event to occur is expressed by the *scattering coefficient*  $\mu_s$  ( $m^{-1}$ ). Moreover, this scattering coefficient can be related to the number density  $N$  ( $m^{-3}$ ) of the scatter medium which expresses the number of particles per unit volume:

$$\mu_s = \sigma_s \cdot N \tag{2.1}$$

where  $\sigma_s$  denotes the *scattering cross-section* ( $m^2$ ) expressing the likelihood of a scattering interaction between a particle and a photon. From Equation (2.1), it follows that higher number densities result in larger scattering coefficients as one would have intuitively expected.

Scattering processes for which the wavelength of incident and scattered light is identical are referred to as *elastic scattering* which is described in greater detail in the following subsection. On the contrary, *inelastic scattering* processes involve an energy exchange between the photon and atom (or molecule).

#### 2.1.1 Elastic Scattering

Elastic scattering is best explained by considering that light is an electromagnetic wave. Upon illumination of an object, this electromagnetic wave induces an oscillation of the electric charges in the sample at the same frequency as the incident wave. From electrodynamics, it is known that accelerated charges emit electromagnetic radiation in all

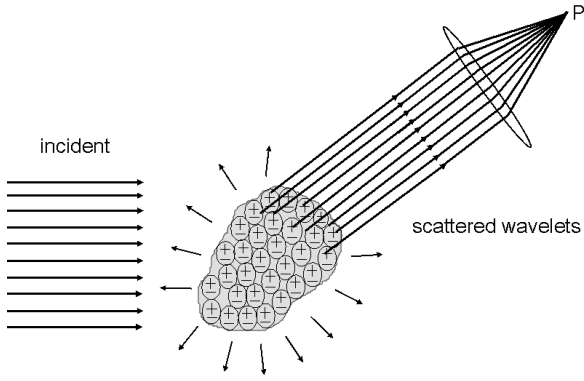


**Figure 2.1:** Illustration of created wavelets which overlap to give the total scattered intensity at the point of interest  $P$ . The scattering particle is partitioned into smaller parts. Image adapted from [8].

directions. Thus, considering that oscillatory motions correspond to accelerations, the oscillating electric charges emit electromagnetic radiation referred to as *scattered light* or *wavelets*.

One important characteristic of these wavelets is their coherent nature, i.e. constant phase relation, which allows the formation of both temporally and spatially stable interference patterns. From a mathematical point of view, interference can be interpreted as the addition of interfering wave functions. This is illustrated in Figure 2.1. In the case of a resulting wave with an amplitude higher than either of the interfering waves, one speaks of *constructive interference*. On the other hand, a lower resulting amplitude is referred to as *destructive interference*. Which of the two cases occurs in a certain point in space is determined by the phase difference of the individual wavelets at that specific point, by the angle of detection as well as by the size of the scattering particles. Based upon the latter, one also distinguishes between different elastic scattering domains by introducing the dimensionless parameter

$$x = \frac{2\pi r}{\lambda} \quad (2.2)$$

where  $r$  denotes the radius of the scattering atom or molecule and  $\lambda$  the wavelength of the incident electromagnetic wave. These different domains are listed in Table 2.1.

The Rayleigh regime corresponds to scattering on particles which are much smaller than the wavelength of the incident light. Here, the different electromagnetic wavelets emitted by the oscillating charges are in phase and variations in the detection angle result in only minor changes of the detected intensity. Furthermore, the magnitude of the scattered electromagnetic wave  $I$  is highly dependent on the particle diameter  $d$  and on the incident irradiation wavelength  $\lambda$  [8], scaling as

$$I \propto \frac{d^6}{\lambda^4}. \quad (2.3)$$

From Equation (2.3), one can see that shorter wavelength are scattered stronger than longer wavelength. However, once the diameter of the particles increases over roughly 10 % of the incident wavelength, Rayleigh scattering no longer offers a realistic description of the scattering processes [8]. Instead, a model referred to as *Mie scattering* takes over for which

**Table 2.1:** Different values of the particle size diameter  $x$  and their corresponding elastic scattering domain.

$x \ll 1$	<b>Rayleigh:</b> Particle size much smaller than the wavelength
$x \approx 1$	<b>Mie:</b> Particle size corresponds approximately to the wavelength
$x \gg 1$	<b>Geometric:</b> Particle much larger than the wavelength

the wavelength of the incident light and the scattering particles' size are roughly of the same dimensions which causes a phase mismatch of the scattered wavelets. The result is constructive and destructive interference, leading to a strong dependence of the scattered intensity  $I$  on the angle of detection. Moreover, in contrast to the Rayleigh regime where the scattered intensity can be expressed through a single equation, an infinite series is necessary in the Mie regime. The third scattering domain is referred to as *geometric scattering* and corresponds to cases in which the incident wavelength is small compared to the particle.

For the samples investigated in this thesis, one has  $x < 1$  and thus, Rayleigh scattering is the domain of interest.

## 2.2 Light Absorption and Emission

A further possibility for photons to interact with matter is through absorption, i.e. a transformation of the photon's energy into internal energy of the absorbing atom or molecule, for instance. Similar to scattering processes described above, the probability per unit length for an absorption event to occur is expressed by the *absorption coefficient*  $\mu_a$  ( $m^{-1}$ ) which in return can be linked to the number density  $N$  of the absorbing medium through the *absorption cross-section*  $\sigma_a$  ( $m^2$ ) in analogy to Equation (2.1).

In most cases, the absorption of a photon results in an excitation of the absorbing matter. However, the second law of thermodynamics states that a closed system (in the case present, the absorbing matter) strives for a state of minimal energy. Hence, the increased internal energy is released again through one of many possible de-excitation processes such as collisions with other atoms or molecules, excited state reactions or fluorescence. For the work presented in this thesis, only the latter is of relevance.

### 2.2.1 Fluorescence

*Fluorescence* is a term referring to the emission of light by an atom or molecule subsequent to the absorption of electromagnetic radiation. More precisely, the excited atom or molecule relaxes back into its ground state by spontaneously emitting a photon whose energy equals the energy difference between the pre-emission state and the post-emission

state. While it is in principle possible for the exciting and emitted electromagnetic radiation to be of same frequency (resonance fluorescence), the emitted radiation most often has a lower energy, i.e. lower frequency, than the incident radiation due to partial de-excitation prior to the emission of the photon; the fluorescence signal is said to be red-shifted. A useful feature of fluorescence for many physical applications is its species sensitive character which results from the energy level structure that is unique to the considered atom or molecule.

## 2.3 Light extinction

Both scattering and absorption processes in the medium through which the electromagnetic wave travels can contribute to light extinction, i.e. fewer photons leaving the medium than were initially sent in. The probability per unit length for an extinction event to take place is equal to the sum of the individual probabilities according to

$$\mu_e = \mu_a + \mu_s \quad (2.4)$$

where  $\mu_e$  ( $m^{-1}$ ) is referred to as the extinction coefficient. Moreover, the extinction cross-section  $\sigma_e$  can also be expressed as a sum of the individual cross-sections according to

$$\sigma_e = \sigma_a + \sigma_s \quad (2.5)$$

through which  $\mu_e$  can be linked to the number density  $N$  of the extinction medium in analogy to Equation (2.1).

For illustration purposes, one can imagine slicing the sample of interest into thin slabs of thickness  $dx$ . Light extinction in a slice then results in a slightly decreased number of photons exiting the slice. Equivalently, one might say the light intensity  $I$ , defined as the power transported through the unit area, is reduced. This reduction in light intensity  $dI$  is readily expressed as ordinary differential equation of form

$$dI = -\mu_e \cdot I \cdot dx. \quad (2.6)$$

Integrating Equation (2.6) yields

$$I(x) = I(0) \cdot \exp\left(-\int_0^x \mu_e(x) \cdot dx\right) \quad (2.7)$$

which is known as the *Beer-Lambert law*. It relates the reduction in light intensity when traveling through a medium to the extinction coefficient and the distance traveled. From Equation (2.6), one can see that the light intensity decays exponentially with both  $\mu_e$  and the distance. A simplification of the Beer-Lambert law occurs when dealing with homogeneous samples of width  $L$  and constant extinction coefficient  $\bar{\mu}_e$  for which Equation (2.7) can be expressed as

$$I(L) = I(0) \cdot \exp(-\bar{\mu}_e \cdot L). \quad (2.8)$$

Two examples of light extinction that are of great practical importance for the thesis presented here are *laser extinction* and *signal attenuation*.

### 2.3.1 Laser extinction

In laser-based diagnostic techniques such as the one presented in this thesis, the loss in intensity due to light extinction according to the Beer-Lambert law greatly influences the signal-to-noise ratio ( $S/N$ ) and thus, the accuracy of the results. The term *laser extinction* here refers to the exponential loss the incident laser light experiences when traveling through the sample.

The effect of laser extinction on the measurements is illustrated in Figure 2.2. In panel (a), a spatial distribution of scattering particles in the form of two peaks is represented. For most light-detecting techniques, the produced scattering signal is expected to scale linearly with the concentration at the point of scattering. However, as the electromagnetic wave travels through the medium, it experiences an exponential loss in intensity over the widths of the peaks as depicted in panel (b). While the first peak reduces the incident light intensity  $I(0)$  by 33%, the second peak causes a smaller overall loss of intensity as only 67% of  $I(0)$  are incident on the second particle-peak. The result of the measurement is illustrated in panel (c) where one notices the significantly smaller intensity of the second peak as compared to the first peak. Furthermore, the measured distribution of intensity is slightly moved towards the left side of the image from which the irradiation entered the sample.

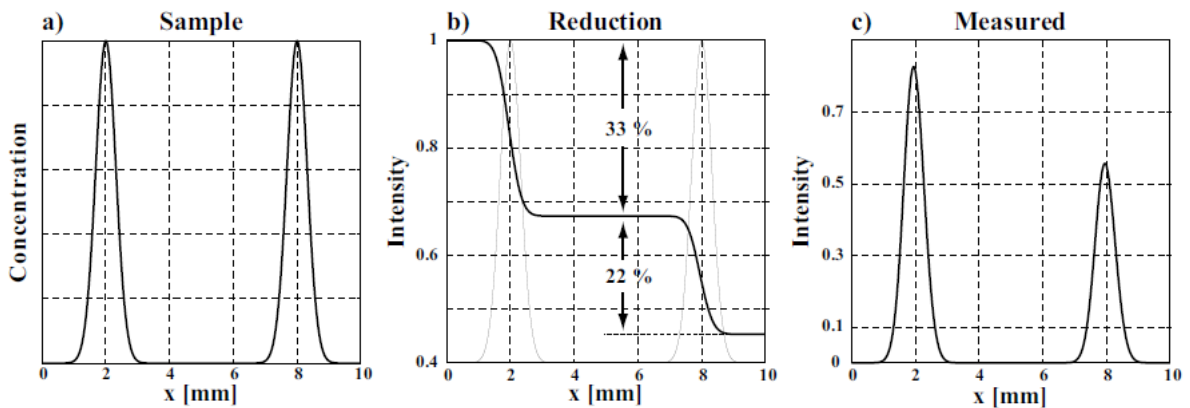


**Figure 2.2:** Measurement inaccuracies due to laser extinction. **a)**: The attenuating particles have a spatial distribution in the form of two peaks. **b)**: Each peak results in an exponential reduction of intensity. **c)**: The measurement results in an inaccurate description of the actual particle distribution. Image with permission from [6].

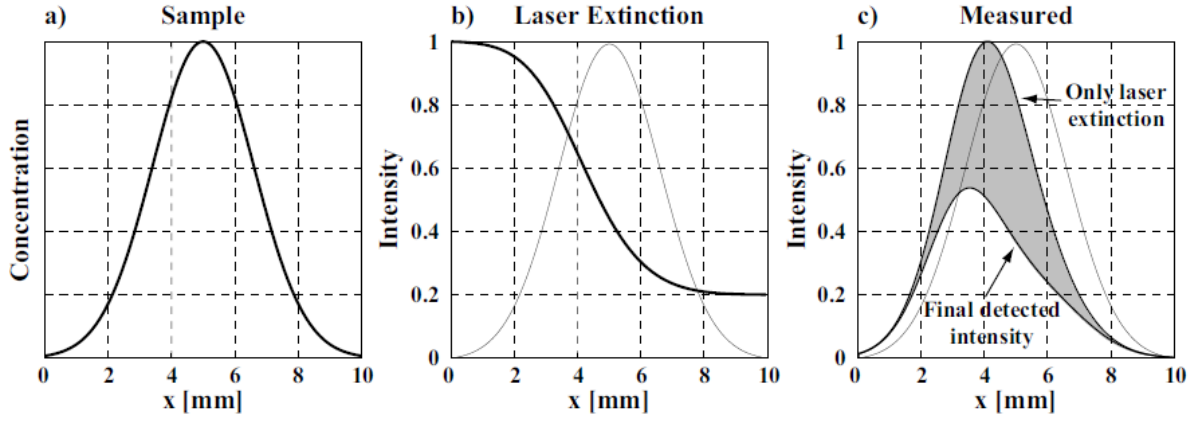


**Figure 2.3:** Illustration of measurement inaccuracies due to laser extinction and signal attenuation. **a)**: The particles causing attenuation have the depicted distribution in the sample. **b)**: The incident irradiance experiences an exponential decrease caused by laser extinction. **c)**: The signal attenuation causes a decrease of the detected signal. Note that the laser extinction graph was used to normalize the curves. Image with permission from [6].

### 2.3.2 Signal attenuation

It is not only the incident laser light that is subject to the Beer-Lambert law but also the generated signal as it travels through the three-dimensional medium. The term *signal attenuation* then describes the exponential loss the signal experiences on its way to the detecting system. Hence, the intensity detected at a position  $x$  can be expressed as

$$I(x) = S \cdot I(0) \cdot \underbrace{\exp\left(-\int_0^x \mu_e dx\right)}_{\text{laser extinction}} \cdot \underbrace{\exp\left(-\int_{z_0}^{z_c} \mu_e dz\right)}_{\text{signal attenuation}}. \quad (2.9)$$

where  $S$  is called the *source function* representing a mathematical characterization of the signal. The position  $z_0$  denotes the location of the irradiating light whereas position  $z_c$  corresponds to the position of the detecting system. The combined influence of signal attenuation and laser extinction is illustrated in Figure 2.3. The symmetrical distribution of light attenuating particles in panel (a) causes laser extinction (b) in analogy to the peaks in Figure 2.2. However, signal attenuation between the light source and detector results in a further signal reduction represented by the gray area in panel (c). Additionally, the bias towards the entrance side of the laser light increases.

## 2.4 Turbidity

In order to be able to quantify the level of turbidity of a sample, different parameters have been introduced of which the *optical depth* and the *scattering order* are of importance for the work presented here.

### 2.4.1 Optical Depth

The *optical depth* (OD) offers a description of how penetrable an object is to light and is defined as

$$OD = \log \left( \frac{I_i}{I_f} \right) \quad (2.10)$$

where  $\log$  denotes the natural logarithm and  $I_i$  and  $I_f$  are the incident and transmitted light intensities respectively. Thus, through comparison with the Beer-Lambert law in Equation (2.7), it follows that one also has

$$OD = \int_0^x \mu_e(x) \cdot dx. \quad (2.11)$$

It is important to note that the OD is a dimensionless parameter. For this thesis, the OD will be employed to quantify the maximum turbidity of samples that can be probed with the setup designed here.

### 2.4.2 Scattering Order

Depending on the number of scattering events  $n$  that a photon has experienced on its way through the sample, the photon leaving the sample is referred to as being of *scattering order*  $n$ . Photons of different scattering orders have distinct applications for which they are best suited. In this thesis, only photons for which  $n = 1$  are of interest. Multiply scattered light, i.e. photons for which  $n \geq 2$ , can limit the measurement accuracy as they lead to false positive signals. Compensating for this effect is vital for the work conducted here and thus, it is appropriate to discuss the influence of multiply scattered light in greater detail.

## 2.5 Multiply Scattered Light

In this thesis, side-scattering detection is employed, i.e. detection of the signal at  $90^\circ$  with respect to the direction of the incident light. For this approach to be applicable, it is assumed that detected photons have only experienced a single scattering event prior to detection which is referred to as the *single scattering approximation*. However, multiply scattered light also reaches the detector resulting in measurement inaccuracies as illustrated in Figure 2.4 for side-scattering detection. Here, different possible trajectories for both singly scattered and multiply scattered photons are displayed:

### Trajectory of Singly Scattered Photons

A Singly scattered photons detected by the camera maintain all information and lead to an accurate characterization of the sample.

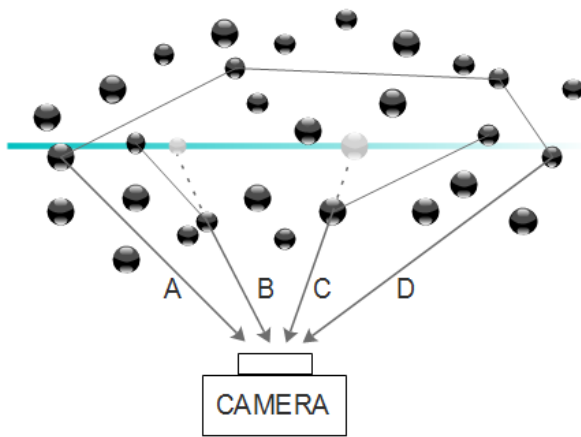


**Figure 2.4:** Illustration of different paths the detected photons might have taken. **A:** Singly scattered light. **B-C:** The multiply scattered light is interpreted as originating from a false position. **D:** Multiply scattered light that cannot be described by the Beer-Lambert law. Image inspired by [6].

### Trajectory of Multiply Scattered Photons

- B A singly scattered photon on its way to the camera experiences a further scattering event that results in a slight change of direction as well as in a change of the detection angle. Consequently, the photon is interpreted to be originating from an incorrect position as indicated by the dotted line.
- C A singly scattered photon that initially would have missed the camera is re-directed onto the detection system due to further scattering events. Once more, it is interpreted as originating from an incorrect position leading to a defective description of the sample of interest.
- D A multiply scattered photon is re-directed into the beam path where it is scattered by an atom or molecule. Even though the resulting signal detected by the camera is interpreted as originating from the correct position, the Beer-Lambert law is no longer valid as the loss of photon energy is not only due to a single scattering event.

Moreover, the number of detected multiply scattered photons is also dependent on setup specific characteristics such as the angle as well as the distance between signal source and detector among others. One way to compensate for the signal contribution from multiply scattered light is *Structured Laser Illumination Planar Imaging* (SLIPI) presented in Chapter 4.

# 3 Dosimetric Procedure and Considerations

Novel developments in the field of radiotherapy have led to advanced techniques that allow the delivery of high doses to the target while simultaneously decreasing the dose absorbed by the surrounding healthy tissue. However, as these techniques often involve moving beams to account for tumor motion, narrow fields or sharp dose gradients, the dosimetric verification of the absorbed dose becomes more challenging [3].

The chapter starts out by describing the samples investigated in this thesis before then elaborating on the dosimetric requirements that the here presented dosimetry technique aims at.

## 3.1 Gel Dosimeter

Even though the probes investigated in this work were not produced as part of the thesis, a short overview of the principal working process shall be given here. For more detailed information on this topic, the reader is referred to [9, 3].

The gel probes initially consist of about 90 % water and 5 % monomers that are sensitive to radiation, i.e. molecules that are capable of binding chemically with other molecules to form polymers, while the remaining 5 % are a gelatine matrix substance [3]. Irradiation of the probe initializes a radiolysis process during which highly reactive radicals are formed through the dissociation of water molecules. These radicals whose number is proportional to the received dose then initialize the polymerization process, i.e. the binding of monomers [10]. The resulting polymers keep growing until two polymers react to form a stable entity. In addition, an oxygen scavenger that is added to the gel prevents the spread of the polymerization process through the whole sample by forming peroxides. Thus, polymerization is confined locally to regions where radiation was absorbed. Furthermore, the use of the gel matrix conserves the spatial distribution of the created polymers, making a later read-out possible [3]. Noticeable characteristics of these gels are their response which was shown to be independent of the energy and of the direction of radiation as well as their soft-tissue comparability [11, 12, 13]. Concerning the refractive index  $n_{gel}$  of the dosimetry gels, no data is available and it is assumed for the work conducted here that  $n_{gel} = 1.4$ . A further important thing to note is that the gels are not

perfectly homogeneous due to polluting particles in the gelatine.

All gel probes irradiated in this work were provided by Sven Bäck and Sofie Ceberg from the division of Medical Radiation Physics at Lund University, Sweden.

## **3.2 Dosimetric Requirements**

One difficulty when trying to define precise requirements is the fact that uncertainties in the determined dose originate from three major contributions [3]:

- 1) The preparation process of the gel sample which depends on the spatial and temporal stability or the temperature during the storage, for instance.
- 2) The irradiation process where dose rate, temperature or contraction of the target volume are of importance.
- 3) The read-out process using MRI or other techniques such as the one presented here.

Consequently, an uncertainty estimation has to be executed individually for each gel composition or read-out technique and there are no generally applicable uncertainty values for when a specific read-out technique can be regarded as well-suited for dosimetry applications. Nonetheless, high spatial resolution and low uncertainties are highly desirable as in any other experiment.

# 4 Structured Laser Illumination Planar Imaging

As described in Section 2.5, multiply scattered light can deteriorate the measurement accuracy when using side-scattering detection techniques in highly scattering media. One way to compensate for this effect is *Structured Laser Illumination Planar Imaging* (SLIPI) which is the topic of this chapter. By going through the designed setup, the principal idea behind the SLIPI technique is first explained. Subsequently, the extraction of the actual SLIPI image, i.e. signal from singly scattered light only, is described in the last section of this chapter.

## 4.1 Experimental Setup

A schematic image of the SLIPI setup is depicted in Figure 4.1 where panel (a) depicts a side view and panel (b) a top view. Moreover, all components are labeled with letters which serve as reference in the following description to provide an adequate illustration of the working principle. As the signal intensity from Rayleigh scattering scales as  $\lambda^{-4}$ , a laser operating at a wavelength of 447 nm which is a short wavelength but still in the visible spectrum is chosen as light source. In order to allow a transport of the designed setup if necessary, all components are fit onto an optical base-plate of 40 cm x 70 cm.

The term *planar laser imaging* (PLI) describes an experimental technique that allows signal generation using a laser sheet instead of the commonly encountered laser beam. The advantage of this approach is its capability to generate a signal originating from within a very thin two-dimensional section of the sample of interest. In order to create the laser sheet, a laser beam is first expanded in all directions using a negative spherical lens (a) of focal length  $f_a = 15$  mm. As the Gaussian beam profile of the laser results in higher measurement uncertainties, e.g. low signal-to-noise ratios (S/N), as compared to a top-hat profile [6], an aperture (b) is placed in the path of the laser light to create a near top-hat intensity profile. The diverging light is collimated again by employing a bi-convex lens (c) whose focal point  $f_c = 225$  cm coincides with that of the negative spherical lens (a). With the help of a positive cylindrical lens (d), the beam is now focused into a laser sheet, i.e. compressed in the horizontal direction, which is clearly visible in panel (b) of Figure 4.1. In the present case, a focal length  $f_d$  of 1000 mm is chosen which

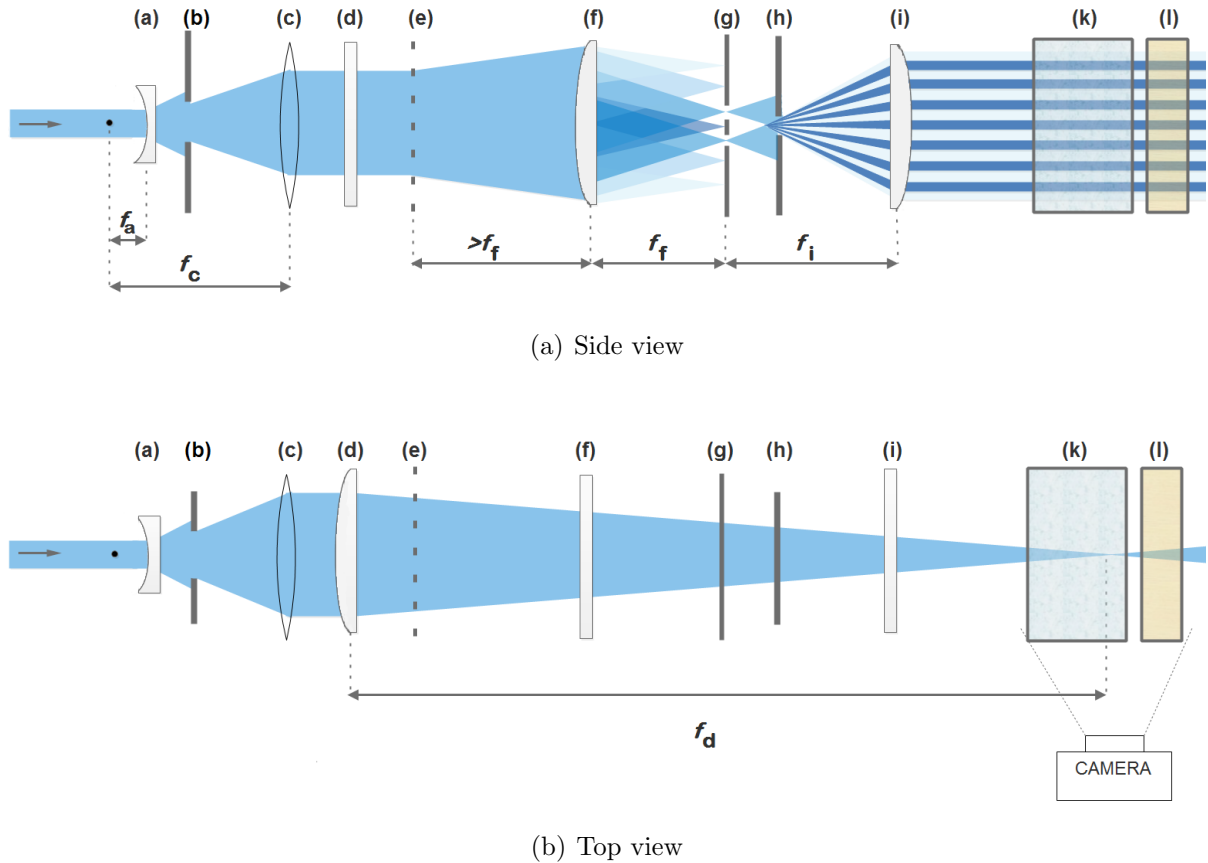


**Figure 4.1:** Schematic side and top view of the built setup. (a) negative cylindrical lens to expand the beam in the vertical direction, (b) aperture to create a near top-hat profile, (c) spherical lens to collimate the light, (d) positive cylindrical lens to compress the laser sheet in the horizontal direction, (e) Ronchi grating, (f) positive cylindrical lens to focus the interference pattern, (g) frequency cutter to block all light but the fundamental peaks, (h) aperture to cut-off the wings, (i) positive cylindrical lens to collimate diverging laser sheet, (k) sample and (l) reference cuvette.

results in a thin laser sheet over a larger distance.

The idea behind SLIPI is to modulate the laser sheet along its height as only singly scattered photons will keep this modulation information. Multiply scattered light does not retain this information, making a suppression of the signal contribution from multiply scattered light in the post-processing possible. The modulation is implemented by employing a grating (e) whose resulting interference pattern is focused again by a positive cylindrical lens (f). In order for the created image to be real, the distance between the grating (e) and the focusing lens (f) needs to be larger than the focal length  $f_f = 150$  mm of the lens (f). The fundamental peaks of this interference pattern correspond to two coherent beams of identical frequency and intensity. More importantly, these fundamental peaks create a perfectly sinusoidal interference referred to as *fringe patterns* when overlapping which in the case present, corresponds to the desired modulation. Hence, a

so called frequency cutter (g) placed at the focal point of the positive cylindrical lens (f) is employed to block out all other peaks apart from the two fundamentals. Following is a further aperture (h) which blocks the outer parts of the two beams that do not overlap. The result is a sinusoidally modulated, yet still diverging laser sheet that passes through the aperture. Finally, with the help of a second positive cylindrical lens (i), the modulated laser sheet is collimated again. The position of this collimating lens is determined by its focal length  $f_i = 300$  mm which needs to correspond to the distance between the frequency cutter (g) and the lens (i). In the region where the laser sheet is thinnest, i.e. around the focal point of lens (d), the sample (k) is placed together with a reference cuvette (l) containing a fluorescent dye. The resulting signal is detected at an angle of  $90^\circ$  with the help of a CCD camera that is only visible in panel (b) of Figure 4.1. With the above described setup, the intensity modulation has a frequency of approximately four lines per millimeter which stretches over a height of about 4 cm in the laser sheet.

## 4.2 Extraction of the SLIPI image

The well-defined spatial frequency  $f_{sig}$  of the modulated laser sheet allows the implementation of a lock-in analysis in order to suppress the signal contribution from multiply scattered light as described in [14]. The signal vector  $S_c$  for each column of the recorded image is given by

$$S_c(R) = A_c(R) \sin(2\pi f_{sig} R + \varphi_c) + B_c(R) \quad (4.1)$$

where  $R$  and  $C$  are the row and column index respectively. Moreover,  $A_c(R)$  represents the modulated part of the signal, i.e. singly scattered photons, whereas multiply scattered light and other interferences lead to an offset  $B_c(R)$ . As the frequency of the modulation stays constant over the whole image, one can form two reference signals  $S_{X,ref}$  and  $S_{Y,ref}$  as

$$S_{X,ref} = \sin(2\pi f_{sig} R + \varphi_{ref}) \quad (4.2)$$

and

$$S_{Y,ref} = \sin\left(2\pi f_{sig} R + \varphi_{ref} + \frac{\pi}{2}\right) \quad (4.3)$$

which only differ by their phase shift of  $\pi/2$ . When multiplied with these reference signals, the signal vector  $S_c$  yields

$$\begin{aligned} S_{X,c}(R) = & \frac{1}{2} A_c(R) \left[ \underbrace{\cos(\varphi_c - \varphi_{ref})}_{(1)} - \underbrace{\cos(4\pi f_{sig} R + \varphi_c + \varphi_{ref})}_{(2)} \right] \\ & + B_c(R) \underbrace{\sin(2\pi f_{sig} R + \varphi_{ref})}_{(3)} \end{aligned} \quad (4.4)$$

and

$$S_{Y,c}(R) = \frac{1}{2}A_c(R) \left[ \underbrace{\sin(\varphi_c - \varphi_{ref})}_{(1)} - \underbrace{\sin(4\pi f_{sig}R + \varphi_c + \varphi_{ref})}_{(2)} \right] + B_c(R) \underbrace{\sin\left(2\pi f_{sig}R + \varphi_{ref} + \frac{\pi}{2}\right)}_{(3)} \quad (4.5)$$

respectively. Comparison with Equation (4.1) illustrates three things; (1) the initially modulated part  $A_c$  now also has an offset that is independent of the frequency  $f_{sig}$ , (2)  $A_c$  is shifted to higher frequencies, namely two times  $f_{sig}$ , (3) the initial offset  $B_c$  is now modulated with a frequency corresponding to  $f_{sig}$ . Hence, a low-pass filter using the initial modulation frequency  $f_{sig}$  as cut-off frequency  $f_c$  eliminates the modulated components. The two new vectors after removal of these contributions are

$$X_c(R) = \frac{1}{2}\tilde{A}_c(R) \cos(\varphi_c - \varphi_{ref}) \quad (4.6)$$

and

$$Y_c(R) = \frac{1}{2}\tilde{A}_c(R) \sin(\varphi_c - \varphi_{ref}) \quad (4.7)$$

where the tilde indicates that the signal has been frequency filtered. For the results presented in this thesis, a gaussian frequency filter is used. Finally, the signal of interest follows as

$$\tilde{A}_c(R) = 2\sqrt{X_c(R)^2 + Y_c(R)^2}. \quad (4.8)$$

It is important to note that implementation of a lock-in algorithm as described above is accompanied with a minor reduction in spatial resolution due to the fact that certain information stays hidden in the shadows of the modulation. On top of that, the low pass filter also contributes to reduction in spatial resolution. The magnitude of the loss is proportional to the inverse of the frequency of the grating employed to create the modulation [14]. For that reason, the modulation chosen here has a rather high frequency of four lines per millimeter. One way to circumvent this problem would be to take three images, each with a modulation phase shifted by  $2\pi/3$ , in which case the signal of interest  $I$  is extracted as

$$I = \sqrt{(I_{-2\pi/3} - I_0)^2 + (I_{-2\pi/3} - I_{2\pi/3})^2 + (I_0 - I_{2\pi/3})^2} \quad (4.9)$$

where  $I_x$  denotes the recorded signal with  $x$  representing the spatial phase.

In order to illustrate the effect the SLIPI approach has on the acquired images, Figure 4.2 displays a comparison between a conventional laser sheet image and a SLIPI image. Here, the modulated laser sheet illuminates a milk-water solution entering from the left and two objects of width 1.5 mm and 3 mm are placed between the laser sheet and the camera as can be seen in Figure 4.2(a). Ideally, the signal at the position of the two ob-

jects should be zero as all light originating from behind the objects is blocked. However, upon examination of Figure 4.2(b) where the image contains both multiply and singly scattered light, one notices that the intensity is highest around the position of the two objects. In contrast to that, the SLIPI image in Figure 4.2(c) which only contains signal contribution from singly scattered light clearly displays a drop in intensity at the position of the two objects. Moreover, the intensity decreases in the propagation direction of the laser sheet. Figure 4.2(d) emphasizes the overall difference between the conventional image and the SLIPI image by plotting the intensity along a horizontal line for both the conventional image (blue curve) and the SLIPI image (red curve). Clearly visible is the continuous loss in intensity in the SLIPI curve which corresponds to the Beer-Lambert law and only at the position of the two objects, the intensity drops down to almost zero. For the conventional image, the intensity stays more or less constant over the whole sample width and only displays distinct peaks at the position of the two objects. Consequently, the algorithm employed here successfully suppresses the signal contribution from multiply scattered light which would otherwise deteriorate measurements.

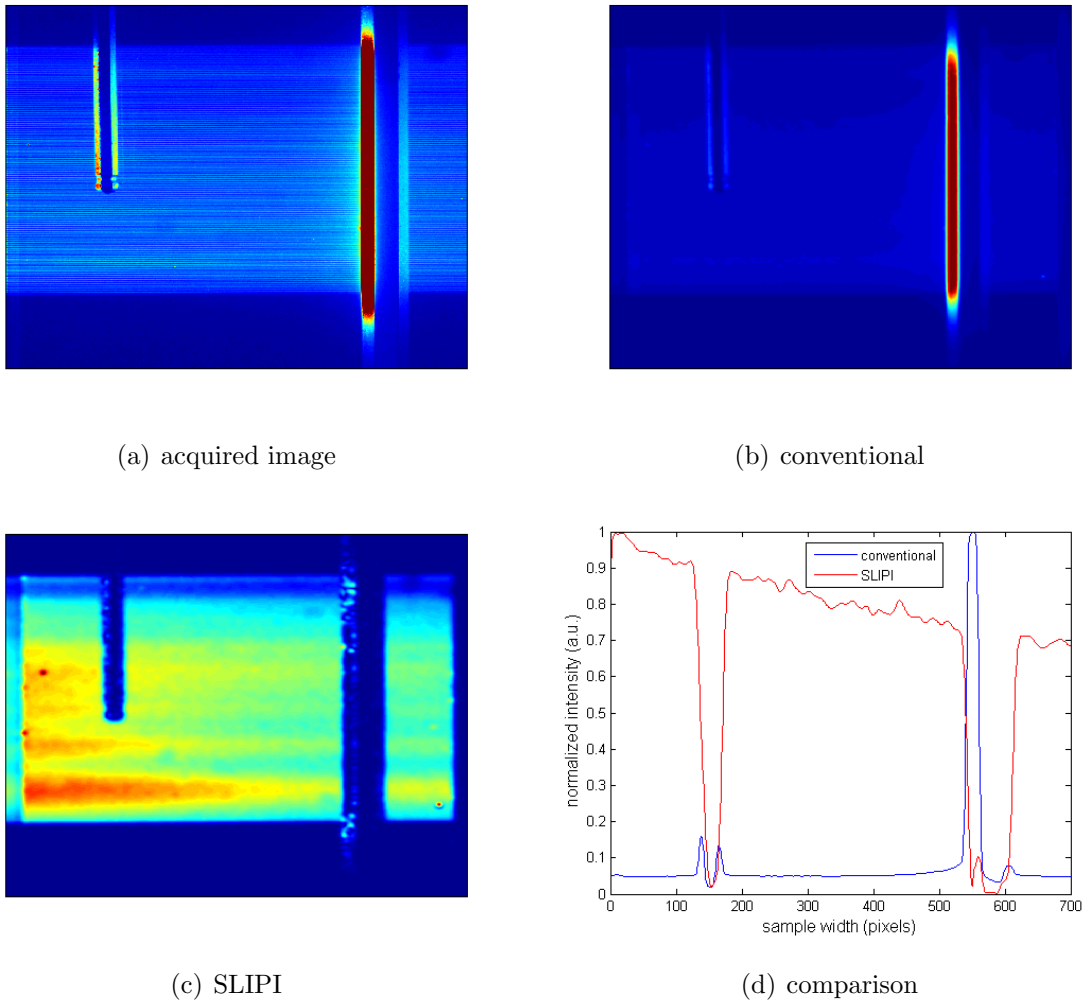


**Figure 4.2:** Comparison of the conventional and the SLIPI approach. From the modulated laser sheet (a), the conventional image (b) as well as the SLIPI image (c) are calculated. The laser extinction according to the Beer-Lambert law and the expected intensity drop at the position of the two objects is only visible for the SLIPI approach as illustrated by the red curve in panel (d) where the intensity is plotted along a horizontal line through images (b) and (c). The blue curve represents the intensity along the same line but for the conventional image.

# 5 Extraction of Local Extinction Coefficient

The aim of this chapter is to provide a detailed description of the extraction method employed to determine the local extinction coefficient  $\bar{\mu}_e$  of the three-dimensional sample. First, the experimental procedure is explained. Subsequently, the formulas implemented in a data post-processing routine to extract the local extinction coefficient  $\bar{\mu}_e$  are presented.

## 5.1 Experimental procedure

The first image recorded at plane  $m = 0$  contains only the fluorescence signal from the reference cuvette which will later serve as incident irradiance on the sample. Based on a “bread-slicing manner”, the sample is then illuminated slice-wise by a modulated laser sheet, with each illumination plane  $m$  being separated by a distance  $dz$  from the position of the previous plane. The whole process is illustrated in Figure 5.1. It is important to note that the plane  $m = 1$  is located as close to the camera as possible such that signal attenuation can be neglected for reasons explained in section 5.2. For all planes other than the plane  $m = 0$ , the camera detects both the scattered light from the sample as well as the fluorescence signal from the cuvette in order to monitor the transmitted irradiance. In order to minimize the influence from background noise, the final image corresponds to the accumulation of ten individual images. With the help of a script that automatically moves the sample and acquires the images, scanning a sample of length 4.5 cm with a step size of  $500 \mu\text{m}$  and image acquisition time in the order of 0.1 s requires only little over five minutes. Subsequent to the data acquisition, the SLIPI data is extracted for each image as described in section 4.2.

The resulting input data for the calculation of the local extinction coefficient is illustrated in Figure 5.2 and consists of two two-dimensional matrices for the incident irradiance  $I_i$  and transmitted irradiance  $I_f$  respectively, plus a three-dimensional matrix containing the SLIPI data of the scatter medium which will hereafter be denoted by  $S_{SM}$ . While the height  $dy$  and width  $dx$  of each voxel are determined by the camera’s pixel size, the length  $dz$  of the voxels corresponds to the separation between the illumination planes.

## 5 Extraction of Local Extinction Coefficient

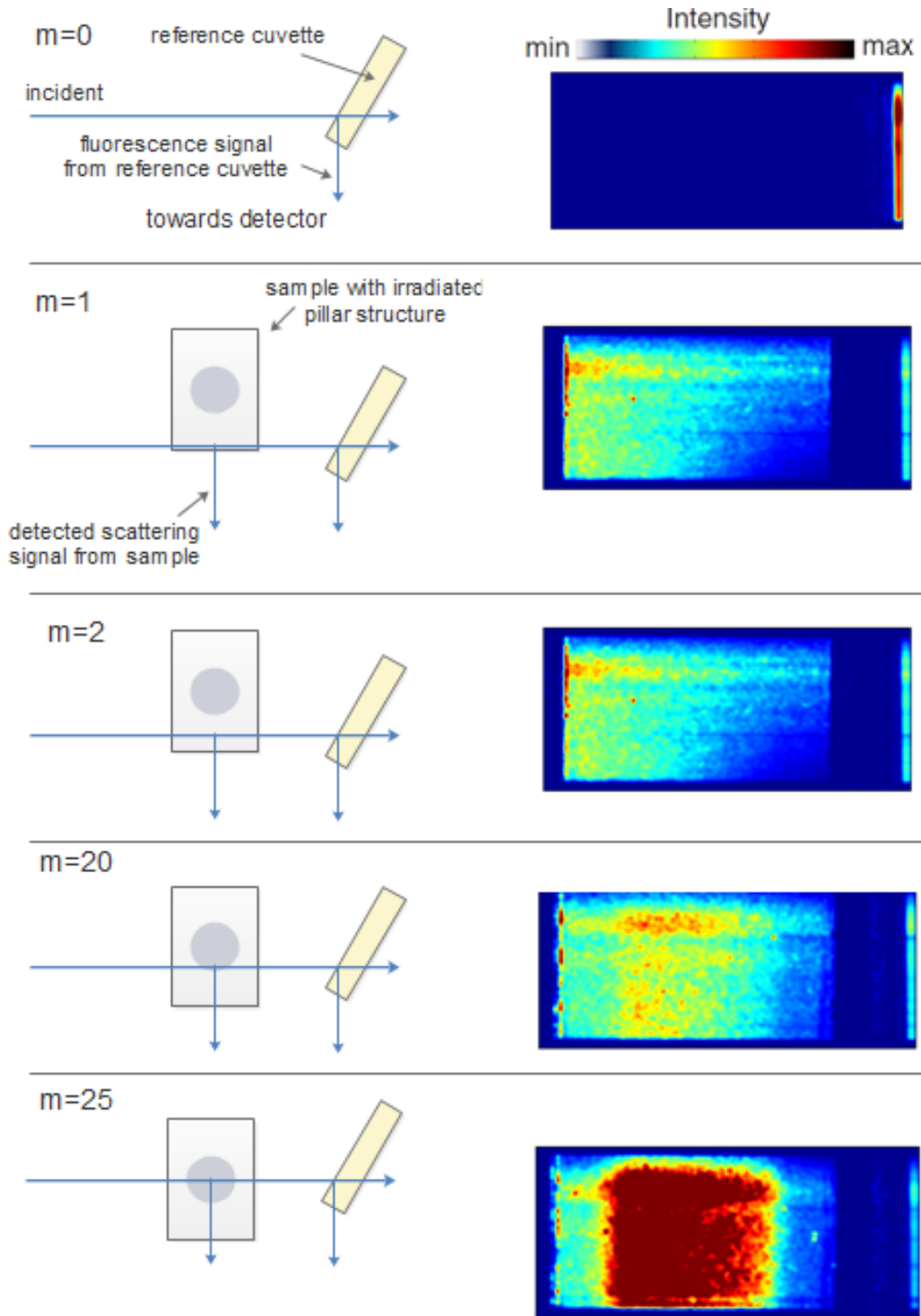


**Figure 5.1:** Illustration of the experimental procedure. The left column depicts a top view of sample and reference cuvette for different layers  $m$  while the right columns contains the corresponding SLIPI image. At plane  $m = 0$ , the camera takes the reference image which only detects the incident irradiance  $I_i$ . The plane  $m = 1$  in the next image includes also the generated signal from the outermost part of the sample where signal attenuation is negligible. The sample is then moved consecutively by a distance  $dz$  closer to the detector until the whole sample has been scanned. Image inspired by [7].

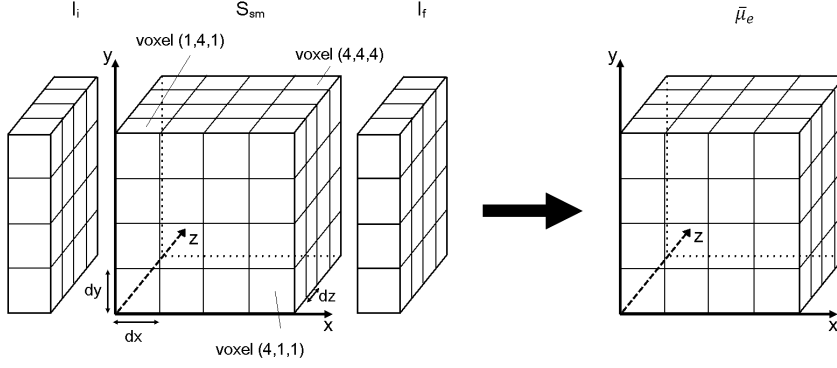


**Figure 5.2:** Illustration of the experimentally acquired input data. The first 2D matrix represents the incident intensity  $I_i$  on the three-dimensional sample. The second two-dimensional matrix contains the exiting intensity  $I_f$  of the sample. From these input matrices, it is possible to extract the local extinction coefficient  $\bar{\mu}_e$  in each voxel of the sample using the algorithm described in section 5.2. Image adapted from [7].

## 5.2 Calculating the extinction coefficient

In order to describe the calculation method employed here, the following theoretical derivation is set up in analogy to the first publication on that subject, [7], using identical nomenclature. Each voxel of the sample in Figure 5.2 can be indexed using the triple  $(k, l, m)$  which denotes the number of voxels in  $x$ -,  $y$ -, and  $z$ -direction respectively.

The detected SLIPI signal  $S_{SM}(k, l, m)$  of the scatter medium in pixels  $k$  and  $l$  of plane  $m$  of the sample can be expressed as

$$S_{SM}(k, l, m) = I_s(k, l, m)K_a(k, l, m)(1 - a(k, l, m)). \quad (5.1)$$

Here,  $I_s(k, l, m)$  denotes the actual irradiance scattered within the considered voxel  $(k, l, m)$ ,  $K_a(k, l, m)$  represents the camera function and  $a(k, l, m)$  the signal attenuation that light experiences when traveling from voxel  $(k, l, m)$  through the sample to the camera. As an experimental determination of the camera function  $K_a$  is likely to introduce errors [7], a final expression for the average extinction coefficient  $\bar{\mu}_e$  independent of  $K_a$  is desirable. The starting point is the signal attenuation  $a(k, l, m)$  which, provided that signal attenuation outside the sample is negligible, can be obtained as

$$a(k, l, m) = 1 - \exp\left(-\sum_{m'=0}^{m-1} \bar{\mu}_e(k, l, m')dz\right) \quad (5.2)$$

where  $\bar{\mu}_e(k, l, m')$  corresponds to the average extinction coefficient in voxel  $(k, l, m')$ . From Equation (5.1), it follows that the scattered irradiance  $I_s(k, l, m)$  is given by

$$I_s(k, l, m) = \frac{S_{SM}(k, l, m)}{K_a(k, l, m)(1 - a(k, l, m))}. \quad (5.3)$$

## 5 Extraction of Local Extinction Coefficient

Moreover, the total extinction of irradiance over a row of voxels, i.e. the difference between incident and transmitted irradiance, can be expressed as the sum over the individual contributions to the scattered light from each voxel in that row:

$$\sum_{k=1}^{k_{max}} I_s(k, l, m) = I_i(l, m) - I_f(l, m) \quad (5.4)$$

where  $I_i(l, m)$  corresponds to the irradiance incident on voxel  $(0, l, m)$  and  $I_f(l, m)$  the exiting irradiance from voxel  $(k_{max}, l, m)$ . From Equations (5.3) and (5.4) it follows that

$$\sum_{k=1}^{k_{max}} \frac{S_{SM}(k, l, m)}{K_a(k, l, m)(1 - a(k, l, m))} = I_i(l, m) - I_f(l, m). \quad (5.5)$$

The camera function  $K_a$  is considered to be independent of  $k$  as the width of each image is considerably smaller than the distance between the sample and camera [7]. Under this assumption, rearranging Equation (5.5) yields

$$K_a(k, l, m) = \frac{\sum_{k=1}^{k_{max}} \frac{S_{SM}(k, l, m)}{(1 - a(k, l, m))}}{I_i(l, m) - I_f(l, m)}. \quad (5.6)$$

Now, inserting Equation (5.6) into Equation (5.3) eliminates the camera function as desired:

$$I_s(k, l, m) = \frac{S_{SM}(k, l, m)(I_i(l, m) - I_f(l, m))}{(1 - a(k, l, m)) \sum_{k=1}^{k_{max}} \frac{S_{SM}(k, l, m)}{(1 - a(k, l, m))}}. \quad (5.7)$$

Moreover, knowing that the first plane ( $m = 1$ ) is located at the outermost part of the sample where signal attenuation is negligible, i.e.  $a(k, l, 1) = 0$ , the scattered irradiance  $I_s(k, l, 1)$  in that first plane can be calculated as all other parameters in Equation (5.7) are recorded with the camera. Next, the irradiance incident on each individual voxel needs to be determined which is implemented column-wise by calculating the difference between the incident irradiance in the previous voxel along the propagation direction and the irradiance scattered in that previous voxel:

$$I(k + 1, l, m) = I(k, l, m) - I_s(k, l, m). \quad (5.8)$$

Here, the incident irradiance on the first column ( $k = 1$ ) corresponds to the incident irradiance recorded on the first image as described in section 5.1. More importantly, the irradiance in neighboring voxels along the direction of the laser sheet propagation can also be determined employing the Beer-Lambert law as follows:

$$I(k + 1, l, m) = I(k, l, m) \exp(-\bar{\mu}_e(k, l, m)dx). \quad (5.9)$$

Thus, by combining Equations (5.8) and (5.9) and solving for the average local extinction coefficient, one obtains

$$\bar{\mu}_e = -\ln \left( \frac{I(k, l, m) - I_s(k, l, m)}{I(k, l, m)} \right) \frac{1}{dx}. \quad (5.10)$$

## 5.2 Calculating the extinction coefficient

All parameters in Equation (5.10) are available and consequently allow the calculation of the extinction coefficient for each voxel in the first plane as described above. In an iterative process, the extinction coefficient is then calculated plane-wise using the calculated values from the previous plane. More precisely, the signal attenuation that scattered light from the second plane ( $m = 2$ ) experiences can be calculated according to Equation (5.2) using the local  $\bar{\mu}_e$  determined for the first plane. Equation (5.7) then yields the scattered irradiance for each voxel in that layer while Equation (5.8) is used to calculate the local irradiance. Lastly, the average local extinction coefficient  $\bar{\mu}_e$  is determined for plane  $m = 2$  from Equation (5.10) and the process is repeated for the following plane.



## 6 Results and Discussion

This chapter presents results from measurements on various samples and explains the steps carried out to verify the accuracy of these results. Figure 6.1 displays a schematic illustration of a sample under investigation in order to clarify how the results are presented. The sample width of 35 mm, the sample depth of 45 mm and the laser sheet of adjustable height span a volume for which the local extinction coefficient  $\bar{\mu}_e$  is to be determined. The side of the sample on which the laser sheet is incident in Figure 6.1 will be referred to as *entrance side*, while the opposite side is referred to as *exit side* from now on. The individual layers for which the images are acquired are parallel to the front window of the cuvette in Figure 6.1 and stacked along the sample depth. The presentation of the calculated extinction coefficient within this volume is implemented in four different ways; The extinction may be presented (1) along a line parallel to the axis labeled “sample width”, (2) along a line parallel to the axis labeled “sample depth”, (3) in a cut-plane through the volume or (4) as a three-dimensional isosurface plot.

Starting out, potential error sources will be investigated that could potentially lead to false signals. In order to compensate for these effects, experimental as well as numerical adjustments are introduced which will be demonstrated. Moreover, a qualitative as well as quantitative verification of the results is achieved using homogeneous milk-water solutions as well as a non-irradiated dosimetry gel which is also homogeneous. Lastly, measurements on irradiated dosimetry gels are presented and different methods to visualize the irradiated structures are investigated.

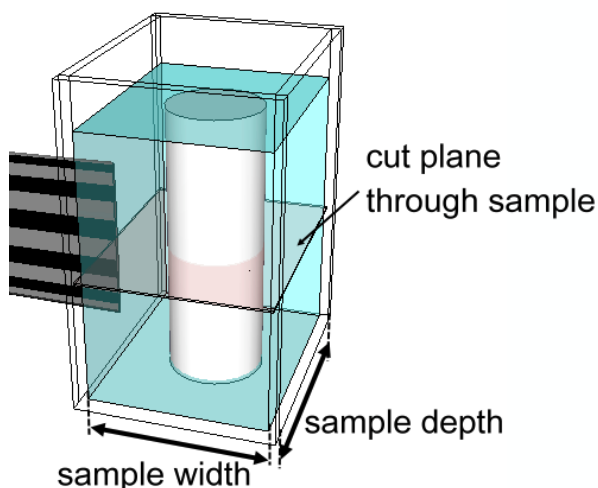


**Figure 6.1:** Illustration of a probed dosimetry gel with irradiated pillar structure. The sample width, sample depth and laser sheet height span the volume within which the local extinction coefficient is determined.

## 6.1 Synthetic datasets

For the subsequent investigation of potential error sources, synthetic datasets are created to support the discussion as they should ideally yield perfect results. The advantage of employing synthetic datasets is the possibility to examine the individual influence of specific error sources whereas measurements conducted are likely to be affected by a combination of different error sources. Of course, in order for the synthetic datasets to correspond to a realistic description of the simulated scenario, the underlying physics has to be known sufficiently well.

As a first step to create a very basic model, the extinction coefficient in each pixel of the synthetic dataset is defined and saved in a matrix. For convenience, the synthetic dataset created is of the same size as the sample volume investigated experimentally. The incident intensity  $I_i$  on the first column of each layer is set arbitrarily to one as calculations should be independent of the absolute value of  $I_i$ . Applying the Beer-Lambert law using the defined extinction coefficient matrix, the incident intensity on each column of the synthetic sample is then calculated consecutively which corresponds to the effect of laser extinction. The transmitted intensity is determined from the intensity incident on the last column of the sample to which the Beer-Lambert law is applied once more.

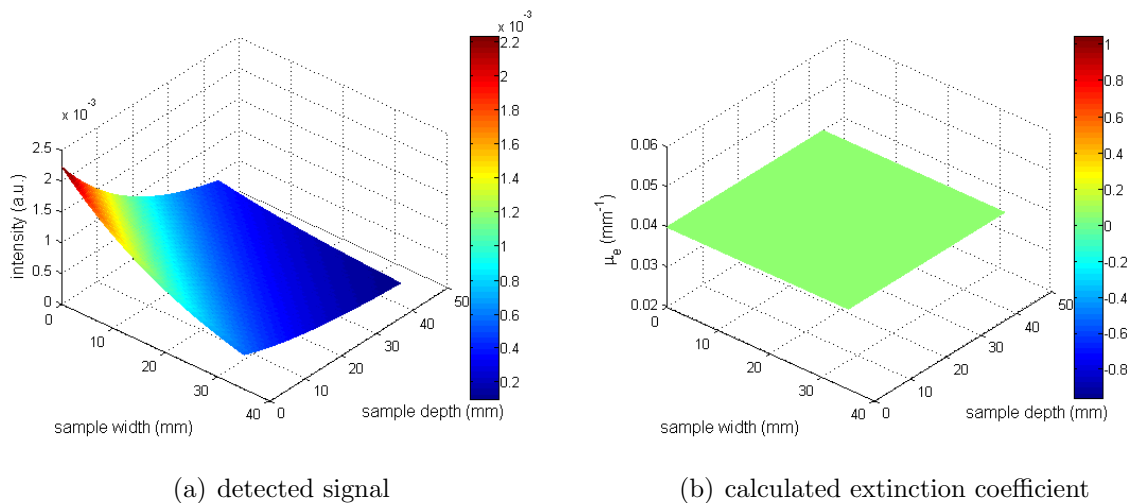


**Figure 6.2:** Detected signal from the synthetic dataset (a) as well as the calculated extinction coefficient (b).

The signal detected from the synthetic dataset corresponds to the light scattered in each pixel, i.e. the difference in intensity between two consecutive pixels which is calculated next. However, the resulting matrix corresponds to the detected signal if only laser extinction was present but no signal attenuation. In order to include the effect of signal attenuation, the laser-extinct signal from the voxels in each layer of the synthetic dataset is reduced by applying again the Beer-Lambert law. More precisely, the exponent in the

Beer-Lambert law now considers the sum over the extinction coefficients of all voxels between the camera and the voxel of interest according to Equation (5.2). The resulting signal from a synthetic dataset with constant extinction coefficient of  $\mu_e = 0.04 \text{ mm}^{-1}$  is displayed in Figure 6.2(a) where one can see the exponential loss in signal as one moves further into the sample. The extinction coefficient determined numerically from that signal using the algorithm described in section 5.2 yields the plot depicted in Figure 6.2(b). As expected, the extinction coefficient is constant throughout the sample. More accurately, maximum deviations from the input of  $0.04 \text{ mm}^{-1}$  are in the order of  $10^{-11} \%$  and are most likely due to truncation errors.

For the following discussion of potential error sources, the basic synthetic model described above is extended where necessary to simulate the influence of specific effects.

## 6.2 Potential error sources

The focus of this section is on experimental error sources that could possibly lead to false signals resulting in inaccurate values of the local extinction coefficient. In order to be able to quantify and describe these influences, homogeneous samples as well as the synthetic datasets described in the previous section are used where necessary. The homogenous samples employed in the verification process are milk-water solutions as well as a non-irradiated dosimetry gel for both of which one would expect a constant extinction coefficient throughout the sample. In the following subsections, the potential error sources investigated for this thesis are addressed individually.

### 6.2.1 Laser fluctuations

As described in section 5.1, the first image taken at plane  $m = 0$  displays only the reference cuvette and serves the purpose of recording the intensity incident on the sample for all planes  $m > 0$ . Consequently, the measured laser extinction according to Equation (5.4) will not correspond to the true value if the laser exhibits significant temporal fluctuations in intensity. Figure 6.3(a) displays the intensity of the modulated laser sheet from five different images taken over a time span of one hour. As one can see, variations between the different curves are barely visible. Additionally, the corresponding standard deviation  $\sigma$  is plotted in Figure 6.3(b) and its mean value corresponds to  $0.56 \%$  of the mean intensity in panel (a). For the measurements conducted in this thesis, these small variations are considered to be negligible which is reasonable considering that the scanning process only takes between five to ten minutes depending on step size and image acquisition time. If necessary, one could however include intensity fluctuations using a second reference cuvette which is placed in front of the sample to monitor the incident laser intensity for each plane individually. In that case, the second reference cuvette would then only

## 6 Results and Discussion

monitor the transmitted laser intensity for each plane.

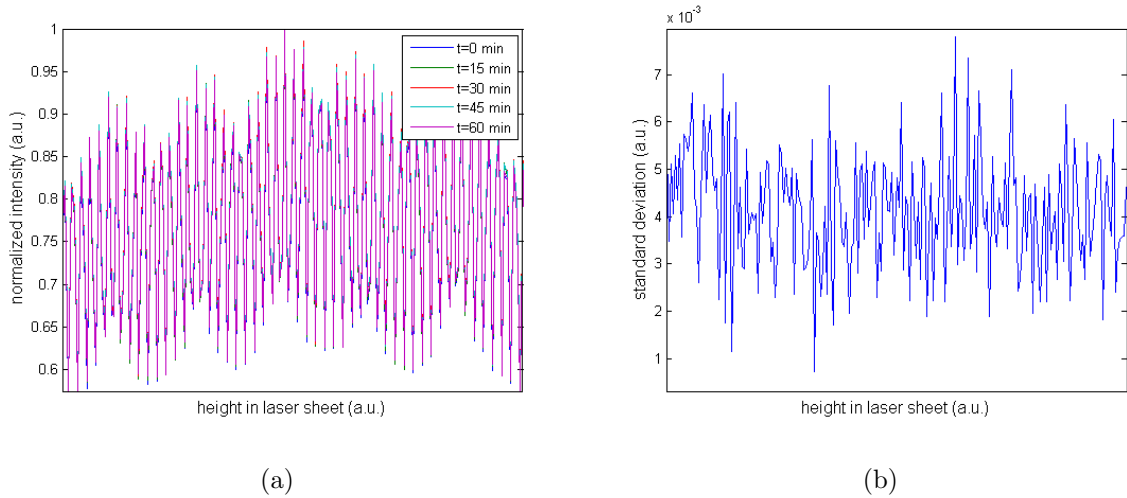


**Figure 6.3:** Illustration of the temporal laser stability. Image (a) depicts the incident laser intensity along the laser sheet at five different times separated by 15 min each. Clearly visible is the intensity modulation whereas differences between the curves are difficult to make out. In panel (b) one can see the corresponding standard deviation.

### 6.2.2 Depth of Field

The *depth of field* (DOF) corresponds to the distance by which the closest and remotest sharp objects in an image are separated. Considering the DOF is of importance for the work conducted here because the optical path length  $l_{op}$  which the signal travels to the camera changes when moving the sample despite the physical distance  $l$  between the laser sheet and the camera remaining constant. Figure 6.4 illustrates this effect which is caused by the refractive index  $n \neq 1$  of the dosimetry gels. While one can assume that in the first layer, the optical path length is identical to the physical distance between the laser sheet and the camera as the signal travels almost only through air, one has to consider that for all other layers, the signal travels through the sample over a certain distance. The optical path length  $l_{op}$  is calculated by multiplying the physical length of the distance traveled in a medium with the refractive index of the medium. More importantly, it follows from Figure 6.4 that the difference in optical path length  $\Delta l_{op}$  between the laser sheet in the first layer  $l_{op}^{(1)}$  and in the last layer  $l_{op}^{(2)}$  can be expressed as

$$\begin{aligned}
 \Delta l_{op} &= l_{op}^{(2)} - l_{op}^{(1)} \\
 &= n \cdot d + l - d - l \\
 &= (n - 1) \cdot d
 \end{aligned} \tag{6.1}$$

where  $d$  denotes the physical length of the sample. With a sample length of  $d = 4.5$  cm and an estimated refractive index  $n_{gel}$  for the dosimetry gels of 1.4, the maximum difference

in optical path length is  $\Delta l_{op} = 1.8$  cm according to Equation (6.1). Thus, as the SLIPI approach described in Section 4.2 requires the modulation of the laser sheet to be detected in all layers of the sample, the full width at half maximum (FWHM) of the DOF should be equal to a minimum of 1.8 cm. For the high frequency line structure created by the setup, the DOF is displayed in Figure 6.5 for different f-numbers  $f_{\#}$  of the camera. The corresponding FWHM are additionally listed in Table 6.1 from which one infers that f-numbers of  $f_{\#} = 11$  or higher are a suitable choice for the here conducted experiments. However, one also has to note that larger f-numbers lead to a reduced signal collection as the aperture is smaller and less light enters the camera.

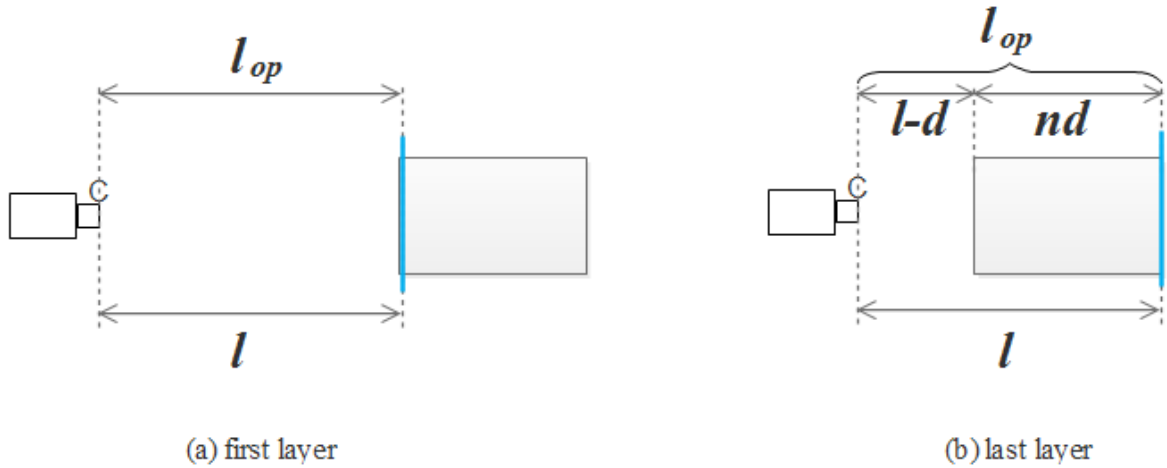


**Figure 6.4:** Illustration of the different optical path lengths for the first layer and the last layer. The laser sheet is depicted in blue. While in the first layer the optical path length  $l_{op}$  is equal to the physical distance  $l$  between camera and laser sheet, one has to take into consideration the refractive index  $n$  of the sample as well as its length  $d$  for all other layers. The camera is denoted by C.

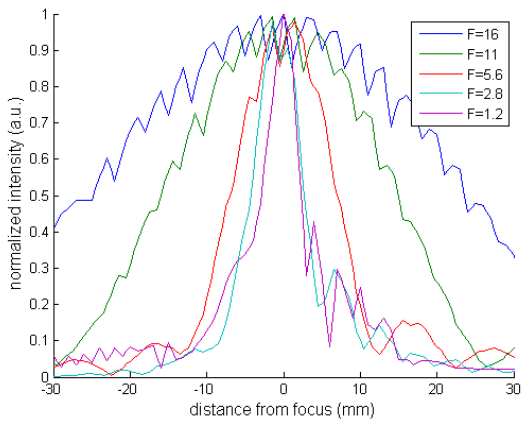


**Figure 6.5:** Depth of field for the modulated laser sheet using different f-numbers of the camera.

A further aspect that needs to be considered is the position of the focus in the sample. For instance, if the focus is chosen to be in the first or last layer, only half of the FWHM is available to cover any change in optical path length  $\Delta l_{op}$  as is illustrated in Figure 6.6.

The consequence would be a signal loss in the layers that do not fall within the FWHM as the modulation of the laser sheet might no longer be detectable. Thus, in order to take advantage of the complete FWHM, a focus position in the middle of the sample is an appropriate choice.

**Table 6.1:** FWHM of the DOF curve for different f-numbers  $f_{\#}$  of the camera objective.

$f_{\#}$	FWHM (mm)
1.2	5.00
2.8	6.95
5.6	14.00
11	31.75
16	48.05

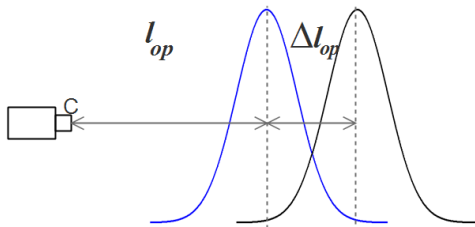


**Figure 6.6:** Illustration of the influence that the position of the focus has on measurements. If the focus of the camera is located in the first layer, the FWHM of the DOF (blue curve) does not cover the full change in optical path length  $\Delta l_{op}$ . Similarly, a focus in the last layer (black curve) does not cover the optical path length  $l_{op}$  in the first layers.

However, it is important to note that despite influencing the signal strength, the DOF has little influence on the calculations provided that the modulation of the laser sheet remains detectable. To illustrate this a little further, a homogeneous synthetic dataset with extinction coefficient  $\mu_e = 0.04 \text{ mm}^{-1}$  is employed. Assuming a gaussian DOF with a FWHM of 3 cm, the signal from the synthetic dataset (red curve in Figure 6.7(a)) is multiplied by the DOF curve which is once focused on the first layer and once on the last layer (black curves). The resulting detected signals from each layer are plotted in Figure 6.7(b). For a focus in the first layer, the detected signal (blue curve) decreases much faster as compared to the case of only signal attenuation (red curve). In the opposite case when the focus is located in the last layer, the detected signal increases the further one goes into the sample (green curve). Despite these different behaviors, the calculations yield accurate results in all three cases with a maximum deviation from the input  $\mu_e = 0.04 \text{ mm}^{-1}$  in the order of  $10^{-11} \%$  which are again interpreted as truncation errors. Considering again Equation (5.7), this result is reasonable as the scattered light  $I_s$  in each voxel is proportional to the laser extinction over the whole line weighted by the signal strength  $S_{SM}$  in that same voxel. Most importantly, the local extinction coefficient  $\bar{\mu}_e$  in Equation (5.10) is therefore independent of absolute intensity values which emphasizes the strength of the approach employed here.

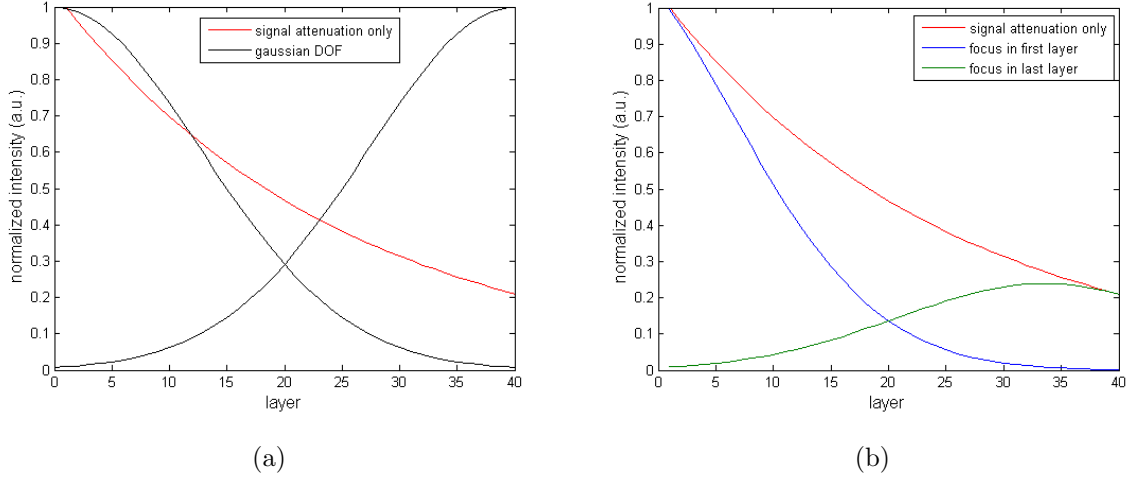


**Figure 6.7:** Image (a) depicts the signal from each layer (red curve) as well as the gaussian DOF with a FWHM of 3 cm centered once on the first layer and once on the last layer (black curves). Multiplying the gaussian DOFs with the red curve yields the blue and green curves in image (b).

Nonetheless, in order to avoid any problems when extracting the SLIPI images, an f-number of  $f_{\#} = 16$  is chosen for all measurements presented here and the camera is focused on the middle layer of the sample.

### 6.2.3 Reflections

As discussed in the preceding subsection, the total laser extinction over one line plays an important role and strongly affects the absolute values of the calculated local extinction coefficients. Consequently, a precise determination of the incident and transmitted light is vital in order to obtain accurate results. The most important aspect that needs to be considered when monitoring the incident and transmitted light are reflection losses introduced by the glass cuvettes. For light incident perpendicularly on a surface with refractive index mismatch, the amount of reflected light  $R$  can be calculated as

$$R = \left( \frac{n_1 - n_2}{n_1 + n_2} \right)^2 \quad (6.2)$$

according to [15] where  $n_1$  and  $n_2$  denote the refractive indexes of the two media. In cases where light is not incident perpendicularly on the surface, one has to consider both polarization and incident angle in the calculations. The reflection coefficients  $r_{tm}$  for transverse electric polarization and  $r_{tm}$  for transverse magnetic polarization are then given by

$$r_{te} = \frac{n_1 \cos(\theta_1) - n_2 \cos(\theta_2)}{n_1 \cos(\theta_1) + n_2 \cos(\theta_2)} \quad (6.3)$$

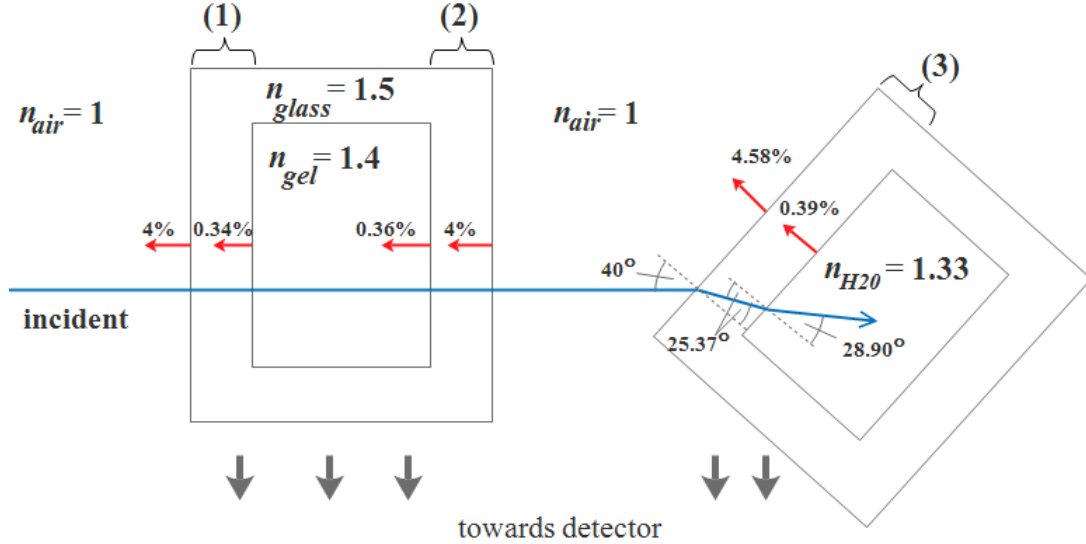


**Figure 6.8:** The amount of reflected light (red arrows) from each relevant surface. The incident laser sheet is marked in blue. For the tilted reference cuvette, the light is assumed to have an equal amount of tm- and te-polarized light.

and

$$r_{tm} = \frac{n_1 \sec(\theta_1) - n_2 \sec(\theta_2)}{n_1 \sec(\theta_1) + n_2 \sec(\theta_2)} \quad (6.4)$$

respectively with the incident angle  $\theta_1$  and the reflection angle  $\theta_2$  [15]. The amount of reflected light  $R$  can be obtained as

$$R_x = |r_x|^2 \quad (6.5)$$

where  $x$  represents the respective polarization. The necessary refraction angle  $\theta_2$  can be calculated according to Snell's law provided that the incident angle  $\theta_1$  is known:

$$n_1 \cdot \sin(\theta_1) = n_2 \cdot \sin(\theta_2). \quad (6.6)$$

The amount of light reflected on each relevant surface in the setup is illustrated in Figure 6.8. For the reference cuvette which is tilted by approximately  $40^\circ$  to avoid reflections re-entering the sample, the amount of transverse electric polarized light and transverse magnetic polarized light is assumed to be equal in which case

$$R = \left| \frac{r_{tm} + r_{te}}{2} \right|^2. \quad (6.7)$$

Here, we consider first the reference image without any sample present and neglect multiple reflections between the two surfaces of each cuvette glass. In that case, the incident light loses a total of 4.95% due to the two reflections on cuvette glass (3) when entering the reference cuvette. Correcting for this effect yields the incident intensity on the reference cuvette  $I_{i,corr}$  which is equivalent to the incident intensity on the the sample cuvette:

$$I_{i,corr} = \frac{I_i}{1 - 0.0495}. \quad (6.8)$$

However, the above corrected incident intensity only corresponds to the intensity incident on the sample cuvette but does not yet correctly represent the incident intensity on the actual sample. From Figure 6.8, it follows that a total of 4.33 % are lost when entering the sample cuvette through cuvette glass (1). Thus, the total incident intensity on the sample  $I_{i,tot}$  is obtained via

$$I_{i,tot} = I_{i,corr} \cdot (1 - 0.0433). \quad (6.9)$$

Next, consider the detected transmitted intensity  $I_f$ . Light propagating through the sample cuvette and entering the reference cuvette experiences a loss of 4.33 %, 4.33 % and 4.95 % on the cuvette glasses (1), (2) and (3) respectively. As the reflections on glass (1) have already been corrected for in the incident intensity, only corrections for reflections on glasses (2) and (3) need to be implemented:

$$I_{f,corr} = \frac{I_f}{(1 - 0.0433)(1 - 0.0495)}. \quad (6.10)$$

To illustrate the importance of considering reflection losses, the signal from a synthetic dataset is adapted to also include reflection losses. Figures 6.9(a) and 6.9(b) display results from the synthetic dataset with an input of  $\bar{\mu}_e = 0.04 \text{ mm}^{-1}$  as well as from a homogeneous milk-water solution, both of which have been calculated without correcting for the above described reflection losses. The images depict the local extinction coefficient in a cut-plane through the sample (compare Figure 6.1). A similar trend of the extinction coefficient is visible in both images; along the side from which the laser sheet entered, i.e. at a sample width of 0 mm, the extinction coefficient decreases slightly as one goes deeper in the sample. However, as one inspects the values going further into the sample along the propagation direction of the laser sheet, one notices an increase in extinction coefficient which is more significant in the last layers as compared to the first layers. At the exit side of the sample, i.e. at a width of 35 mm, the extinction coefficient increases for deeper layers. The highest value of the extinction coefficient can be found at the cross-section of the plane with highest laser extinction and the plane with highest signal attenuation. One distinct difference between the results from the synthetic dataset and the milk solution are the ‘‘ravines’’ that pervade the extinction coefficient from the milk solution of which the most significant one is located at a sample width of approximately 10 mm. It is most likely caused by a polluting particle on the cuvette glass facing the camera which blocks the signal originating from voxels located behind the polluting particle. One can state that this observation illustrates the sensitivity of the technique to polluting particles and thus, the cuvettes are cleaned thoroughly before all future measurement conducted here.

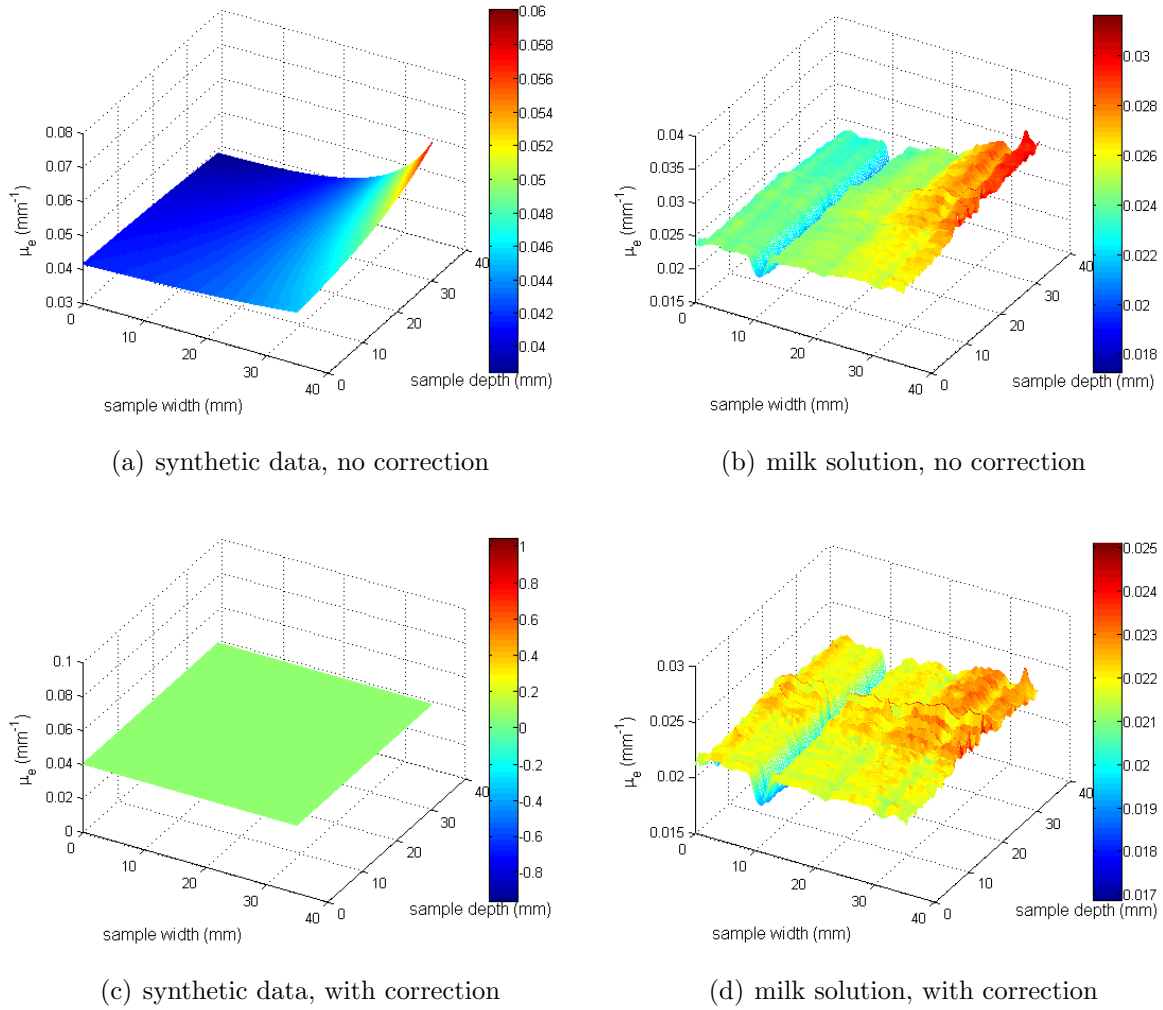


**Figure 6.9:** Extinction coefficient in a plane through the sample for synthetic data (panels (a) and (c)) as well as for a milk-water solution (panels (b) and (d)). The first row does not include a correction for reflections whereas it is incorporated in the second row.

Despite expecting a constant extinction coefficient throughout the sample for both the synthetic data and the milk solution, values vary significantly with a maximum deviation from the input ( $\bar{\mu}_e = 0.04 \text{ mm}^{-1}$ ) of roughly 50% for the synthetic dataset. Thus, correcting for reflection losses is necessary and results including a correction are displayed in Figures 6.9(c) and 6.9(d). The synthetic dataset gives perfect results matching the input value with maximum deviations in the order of  $10^{-11} \%$  as before. Concerning the milk solution, one notices two important things; (1) the steep gradient seen in Figure 6.9(b) is reduced significantly making the plot look far more even and (2) the extinction coefficient in the plane is clearly shifted to lower values. Both observations illustrate how important the accurate determination of the incident and transmitted intensities are. Despite these improvements after correcting for the losses due to reflections, the milk solution still seems to bear a slightly increasing extinction coefficient as one moves closer to the exit side of the sample which is best visible in the last layers. In order to investigate this

behavior, effects of a reflected wave from the exit side of the cuvette (cuvette glass (2) in Figure 6.8) are simulated. Assuming that the reflected wave maintains the modulated structure, it could very well be that the counter-propagating wave leads to signal that is not filtered by the SLIPI approach and results in an increase in detected signal which would be strongest close to the exit side of the laser sheet. As higher signals are equivalent to higher extinction coefficients, this could explain the higher extinction coefficient along the exit side.

The reflected wave is first implemented in a synthetic dataset of constant extinction coefficient  $\mu_e = 0.04 \text{ mm}^{-1}$  by determining the amount of light in the last column of the sample and calculating the amount of reflected light which is equivalent to 4.33%. The amount of reflected light is then distributed according to the Beer-Lambert law and in a direction counter-propagating the laser sheet. The signal detected from the reflected wave is determined by calculating the difference between neighboring voxels in the propagation direction of the wave and is subsequently added to the original signal. The calculated extinction coefficients of the synthetic sample with reflected wave are presented in Figure 6.10(a) where a cut-plane through the sample is considered. One notices that the extinction coefficient increases the further one moves into the sample and is clearly over-estimated along the exit side of the sample. Its highest extinction coefficient is located in the last column of the last layer which corresponds exactly to the behavior observed in the milk solution (compare Figure 6.9(d)). In order to compensate for the effect of a reflected wave, the following iterative procedure is implemented:

- a) Determine a first approximation of the extinction coefficient  $\mu_{e,approx}$  by not considering the reflected wave.
- b) Determine the intensity in the last column of the sample which is equivalent to 104.33% as it includes a reflected wave of 4.33%. From this value, calculate the intensity of the reflected wave.
- c) Determine the additional intensity contribution in all previous columns by applying the Beer-Lambert law in counter-propagating direction using  $\mu_{e,approx}$  calculated in step a).
- d) Subtract the additional intensity contribution from the signal in each voxel of the sample.
- e) Calculate  $\mu_e$  and if necessary start over with step b) using  $\mu_e$  as an improved estimation of the extinction coefficient.

Applying this algorithm to the synthetic dataset yields Figure 6.10(b) after the first iteration. In contrast to Figure 6.10(a), the extinction coefficient is now under-estimated

## 6 Results and Discussion

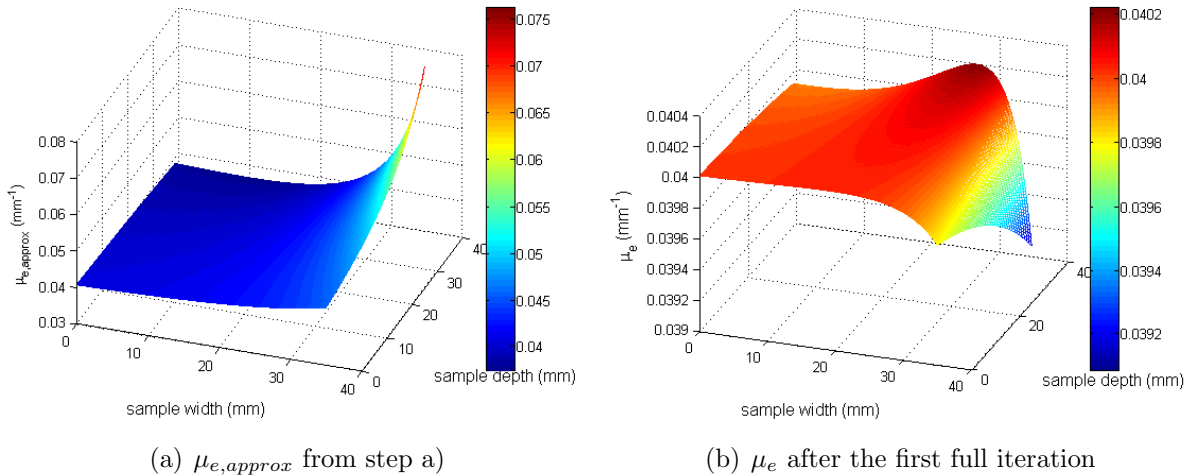


**Figure 6.10:** Illustration of the resulting extinction coefficient for a synthetic dataset from the iterative procedure that compensates for a reflected wave. Panel (a) depicts the first approximation of  $\mu_e$  that is calculated without considering the reflected wave. These values are used to correct for the reflected wave and the resulting extinction coefficient is displayed in panel (b).

at the exit side of the laser sheet which can be explained as follows; The first approximation  $\mu_{e,approx}$  in Figure 6.10(a) included an over-estimated extinction coefficient along the exit side of the sample. Thus, the signal contribution from the reflected wave is also over-estimated. Consequently, when subtracting the intensity contribution of a reflected wave from the original signal in step (e), the signal is reduced by slightly too much. In the following calculation of the extinction coefficient, this results in an under-estimated extinction coefficient along the exit side of the sample. A further iteration would again yield a slightly too high extinction coefficient and so on. Most importantly however, the absolute deviation from the input value decreases with each iteration which can be seen in Table 6.2 where the maximum deviation is listed for several iterations.

**Table 6.2:** Maximum deviation from the input value  $\mu_e = 0.04 \text{ mm}^{-1}$  when using the iterative process to compensate for a reflected wave. All values in %.

first approximation	iteration 1	iteration 2	iteration 3
90.3289	2.2833	0.0935	0.0037

Applying the algorithm to the experimentally obtained dataset yields the plots depicted in Figures 6.11(a) and 6.11(b) which correspond to the results after the first and third iteration respectively. A first thing one notices is that the overall shape of the plot remains unchanged as compared to Figure 6.9(d), i.e. the extinction coefficient still increases towards the exit side and most noticeably in the last layers. Even though the plot is

slightly shifted to higher extinction coefficients as compared to 6.9(d), there is almost no variation between the results for the individual iterations. Figure 6.11(c) illustrates this fact by displaying the difference  $\Delta\mu_e$  between the extinction coefficient after the first iteration and the extinction coefficient after the third iteration. The variations are close to zero for the most part and vary only in the last layers with values in the order of three magnitudes smaller than the absolute value of the extinction coefficients. It is therefore concluded that any influence from counter-propagating waves caused by reflections on cuvette glass (2) are negligible if at all present.

Based on the above described investigation, losses due to reflections are compensated for in all of the following measurements whereas the algorithm used to include the effects of a possible reflected wave is discarded. Consequently, a valid explanation for the slight increase in extinction coefficient towards the exit side observed in Figure 6.9(d) is still to be determined.

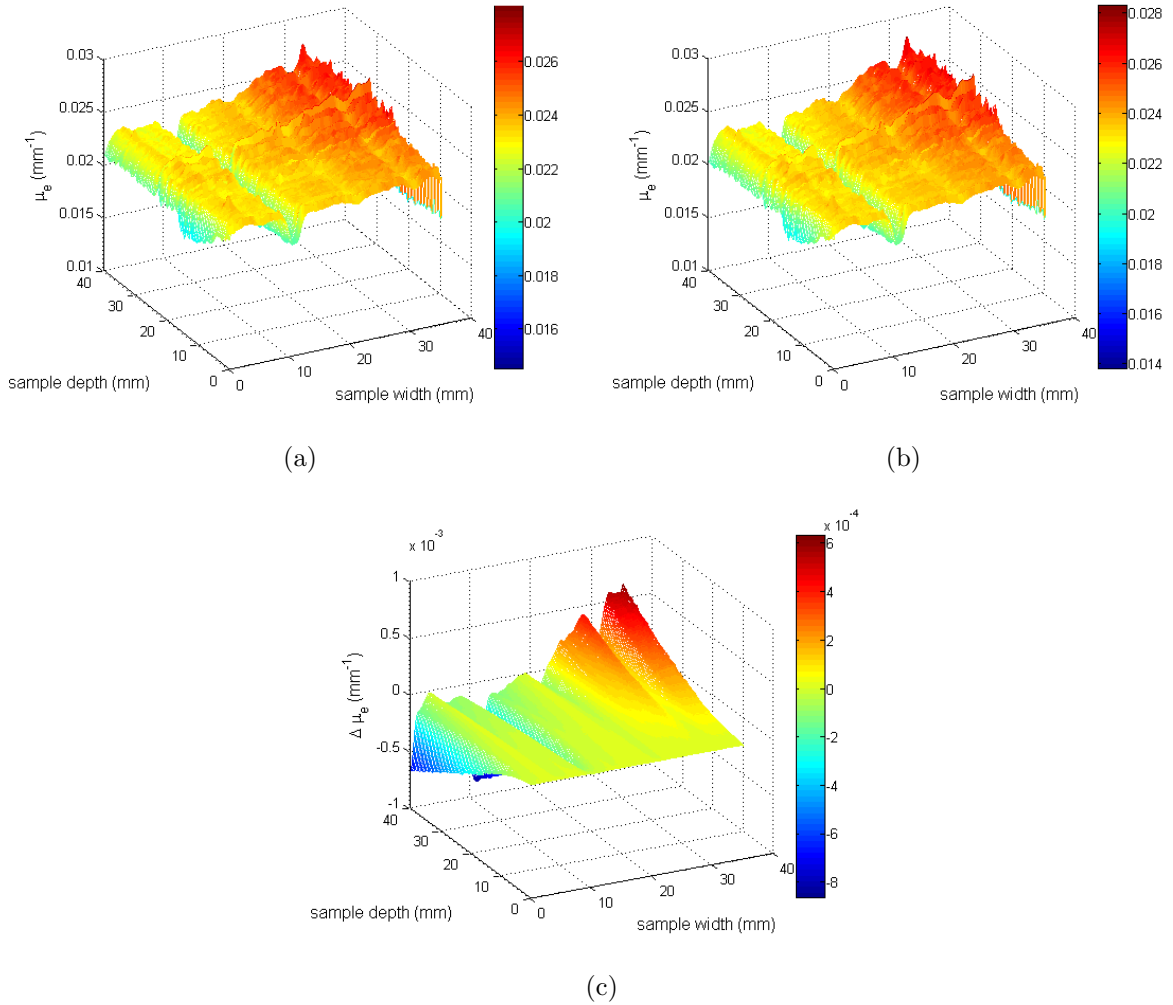


**Figure 6.11:** Illustration of the calculated extinction coefficient after the first (a) and third (b) iteration of the compensation algorithm for a reflected wave when applied to the experimental dataset. Panel (c) depicts the difference between images (a) and (b).

### 6.2.4 Vignetting

The term *Vignetting* most commonly refers to a decreasing intensity towards the outer edges of an image and is caused by varying acceptance angles for the signal from different points in space. In the case present, the glass cuvettes may also limit the acceptance angle as illustrated in Figure 6.12. Closing the aperture of the camera objective, i.e. choosing a higher f-number, is often a convenient mean to compensate for this undesired effect if necessary. Despite having chosen the highest f-number of the employed objective for all measurements presented here, it is still crucial to examine if optical vignetting is an issue as it could potentially falsify signal intensities.

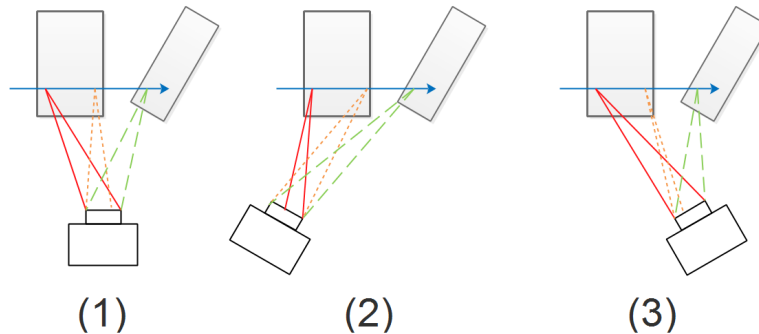


**Figure 6.12:** The acceptance angle for the signal depends on the position in space from where the signal originates as well as on the camera position. In the setup used for measurements in this thesis, the glass cuvette may also limit the acceptance angle as is illustrated by the dotted orange line for camera positions (1) and (3), for instance.

In order to investigate the relevance of vignetting, measurements are conducted for three different camera positions as indicated in Figure 6.12. The sample investigated is a dosimetry gel with an irradiated pillar structure as depicted in Figure 6.1. The gel had been irradiated from below using a beam with gaussian intensity profile. Thus, the extinction coefficient in a layer cutting through the pillar structure should yield a gaussian-like curve as well while expectations are a constant extinction coefficient in the first layers. Figure 6.13 displays the results where the plots correspond to the extinction coefficient along a line through the sample in the direction of the laser sheet propagation. The first layer experiences a distinct drift for camera positions (2) and (3) in the form of an increasing extinction coefficient the further one penetrates into the sample. In the same layer, camera position (1) yields a more constant extinction coefficient without any particular drift being noticeable. The small fluctuations along all three plot lines can be explained by the limited homogeneity of the dosimetry gel as mentioned in section 3.1. Upon inspection of the results for a layer through the pillar structure, one notices that camera position (1) again yields the best results; calculations should result in an equal extinction coefficient to both sides of the irradiated structure which is only true for the blue curve in Figure 6.13(b) corresponding to camera position (1). Both camera positions

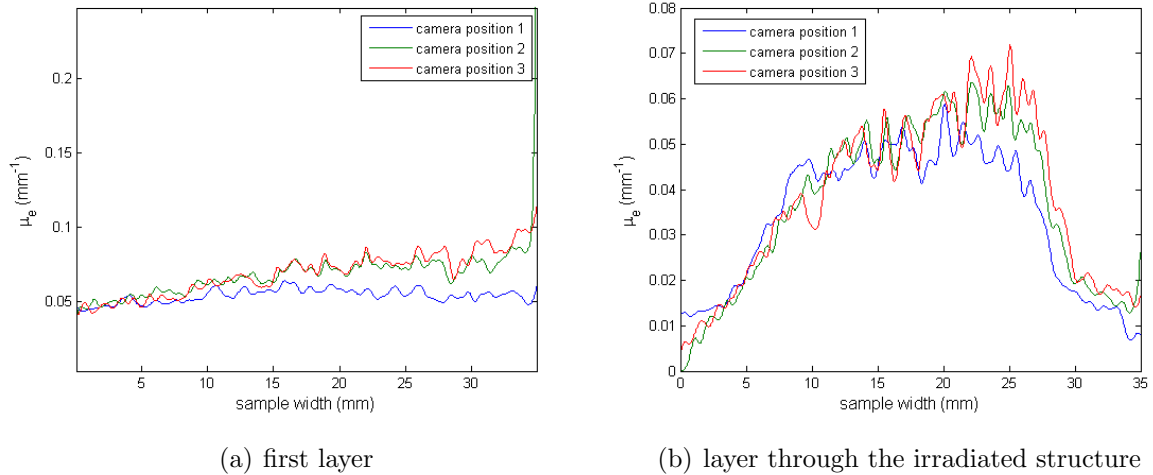


**Figure 6.13:** Illustration of the influence of different camera positions on the results.

The plots display the extinction coefficient along a line in the direction of the laser sheet propagation for two different layers.

(2) and (3) generate an extinction coefficient that is lower on the entrance side of the sample than on the exit side. On top of that, as the beam used to irradiate the polymer gel had a Gaussian beam profile, one expects a similar shape to be visible in a cut-line through the irradiated structure. However, only the blue curve displays a symmetrical behavior whereas the plots for camera positions (2) and (3) are skewed and have a peak that is shifted towards the exit side of the laser sheet.

As a conclusion, vignetting could very well be responsible for the slight increase in extinction coefficient towards the exit side which was observed in Figure 6.9(d) but could not be compensated for by considering a reflected wave. Based on the above stated results, camera position (1) is employed for all further measurements conducted.

### 6.3 Verification of results

Taking into consideration the previously discussed error sources, measurements are implemented to provide both a qualitative as well as quantitative verification of the results.

The former is achieved by proving that for a homogeneous sample, the result is indeed a constant extinction coefficient when implementing the corrections described in the previous section. Figure 6.14(a) displays such a plot for a homogeneous milk solution of average extinction coefficient  $\bar{\mu}_e = 0.0079 \text{ mm}^{-1}$ . Other than the small number of spikes which are most likely caused by polluting particles in the solution, the extinction coefficient can be considered as constant which is regarded as a qualitative confirmation of the results. A quantitative verification is achieved by conducting measurements on multiple milk-water solutions of different milk concentrations. As the extinction coefficient is expected to scale

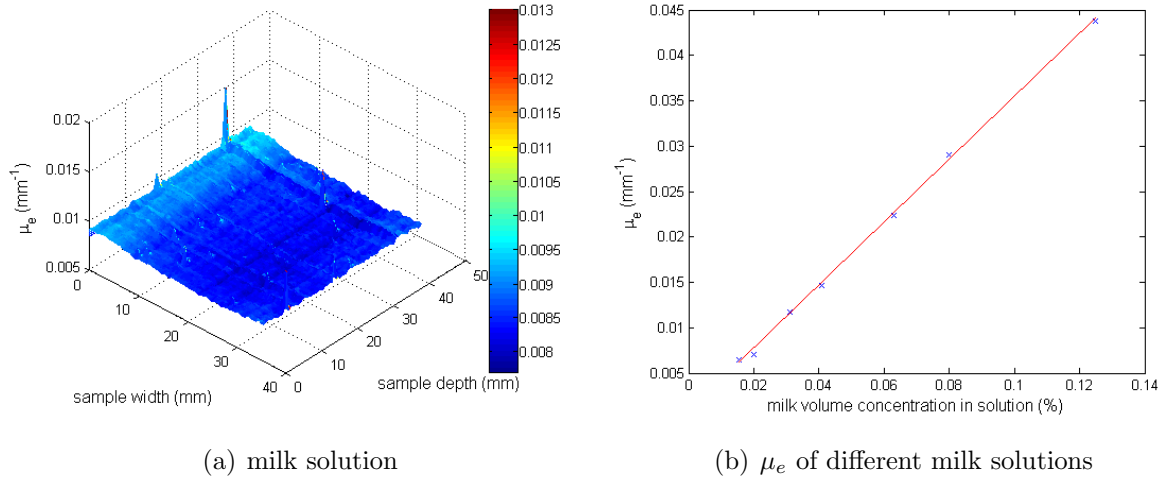


**Figure 6.14:** Illustration of the quantitative and qualitative verification of results.

Panel (a) displays a constant extinction coefficient throughout the whole plane except for a few spikes that are caused by polluting particles. In panel (b) one can see that the data points are in good agreement with the linear model.

linearly with concentration, plotting the determined extinction coefficient as a function of the respective relative concentration should ideally yield a linear slope going through the origin. The corresponding plot is displayed in Figure 6.14(b) and a linear regression yields

$$\mu_e = 0.3466 \frac{1}{\%} \cdot C + 0.0008 \frac{1}{\text{mm}} \quad (6.11)$$

where  $C$  denotes the volume concentration of milk in the milk-water solution in percent. Due to the relatively small offset and the fact that the data points are agreeing well with a linear model, the result is interpreted as a quantitative verification of the extinction coefficients determined.

## 6.4 Probing of different dosimetry gels

In this section, measurements on actual dosimetry gels are presented and the irradiated structures are visualized both in two as well as in three dimensions. Starting out, the dosimetry gel with an irradiated pillar structure already used in Section 6.2.4 is examined more thoroughly before samples with more complex structures, i.e. overlap of multiple irradiation beams, are investigated.

### 6.4.1 Dosimetry Gel with Pillar Structure

The dosimetry gel examined first here was irradiated from the bottom, creating a pillar-like structure as is schematically illustrated in Figure 6.1. As mentioned before when

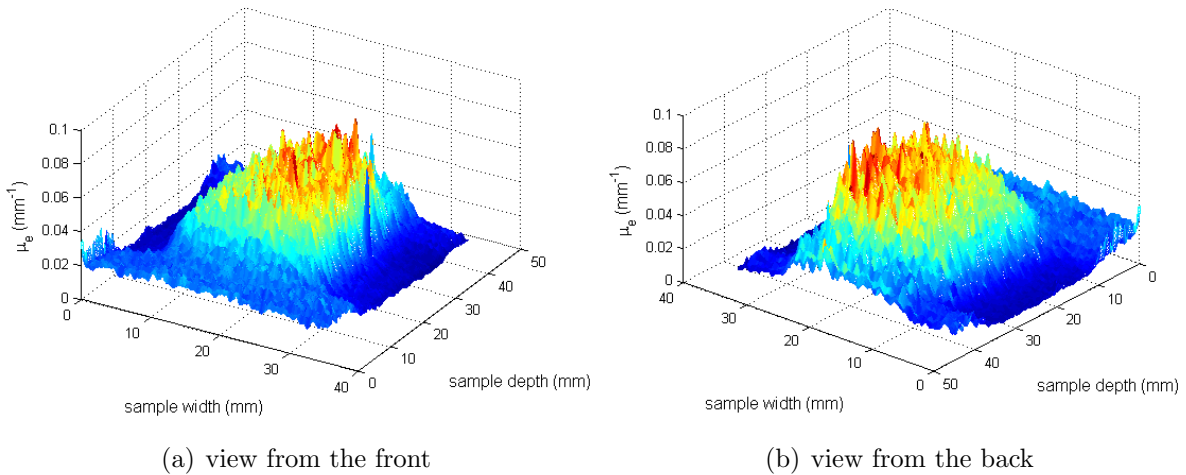


**Figure 6.15:** Illustration of the extinction coefficient in a cut-plane through a dosimetry gel with irradiated pillar structure. The cut-plane is displayed as viewed from the front of the cuvette (a) as well as from the back of the cuvette (b). One notices that behind the pillar structure, the values do not decrease back to the values in front of the pillar.

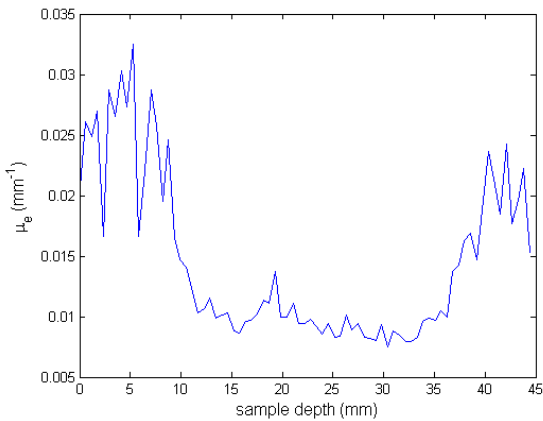


**Figure 6.16:** Illustration of the extinction coefficient along the entrance side of the sample. The values corresponding to depths over which the pillar structure extends are much lower but also less noisy than in the regions in front and behind the pillar.

investigating the effect of vignetting in Section 6.2.4, the pillar should have a profile resembling a Gaussian. Moreover, the extinction coefficient of the gel surrounding the pillar structure is expected to be of constant value. Figure 6.15(a) displays the extinction coefficient in a cut-plane through the sample where the pillar structure is clearly visible in the form of increasing extinction coefficients towards the middle of the sample. As expected, the first layers display a constant extinction coefficient with only minor fluctuations due to the intrinsically limited homogeneity of the gel (see Section 3.1). Moreover, the value of the extinction coefficient is identical to both sides of the pillar structure for all depths. However, when inspecting the same cut-plane from the back as depicted in Figure 6.15(b), one notices that the extinction coefficient behind the pillar does not decrease all the way to the same value as in the first layers. Furthermore, a discrepancy is observed between the value of the extinction coefficient in the first layers and to both sides of the pillar structure where it is lower. Figure 6.16 illustrates this effect by plotting the extinction

## 6 Results and Discussion

coefficient along the entrance side of the sample. While the average extinction coefficient in the first layers has a value of  $0.024 \text{ mm}^{-1}$ , it drops down to  $0.01 \text{ mm}^{-1}$  besides the pillar before increasing again in the last layers. A further observation is that the result seems to be less noisy besides the pillar structure as compared to the first and last layers. In order to explain these effects, further measurements have to be conducted which are not part of this thesis due to the limited time frame but will be discussed in Section 7.

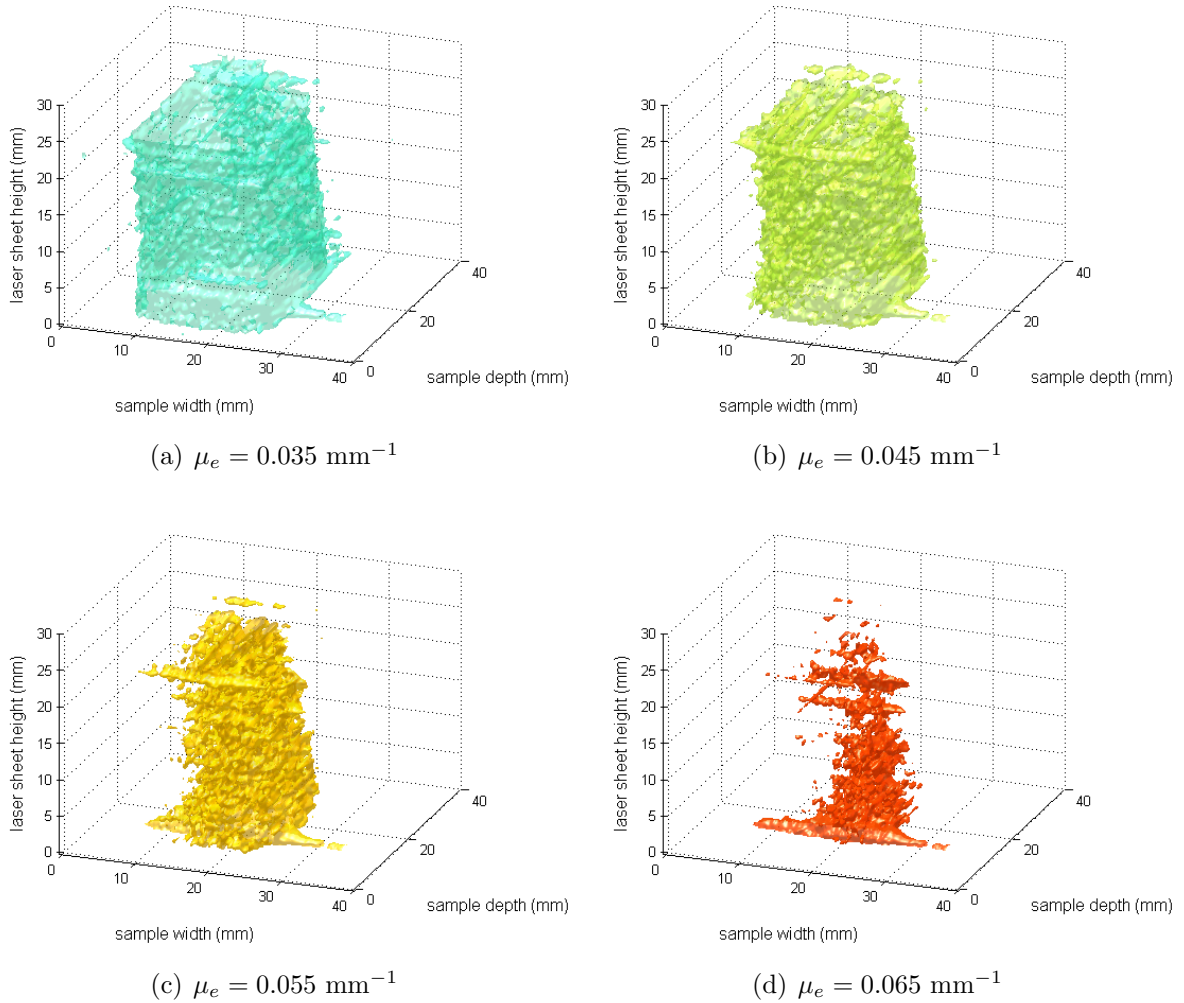


**Figure 6.17:** Visualization of the pillar structure in the form of isosurface plots for different values. As one can see, the pillar diameter increases for decreasing values of the extinction coefficient.

A further possibility to visualize the results and thereby examine the irradiated structure is in the form of three-dimensional isosurface plots. Figure 6.17 depicts the irradiated pillar structure for four different isosurfaces of values  $0.065 \text{ mm}^{-1}$ ,  $0.055 \text{ mm}^{-1}$ ,  $0.045 \text{ mm}^{-1}$  and  $0.035 \text{ mm}^{-1}$  respectively. As one can see, the pillar is centered about the midpoint of the sample and has itself an increasing width for decreasing values of the isosurface which is reasonable considering the Gaussian-like profile, i.e. highest values

are located in the center. However, one also notices some image artifacts which are most noticeable in Figure 6.17(d) where the image displays a broadened structure at the bottom of the pillar whereas the structure disperses more and more towards the top of the image. In addition, the isosurfaces themselves are not perfectly smooth but display some variations.

In conclusion, the new approach is able to create a quantitatively correct visualization of the irradiated pillar structure in the sample which substantiates the great potential of the new technique. However, there are still some discrepancies between the expected behavior and observed results which require further investigations.

### 6.4.2 Probing of spatially overlapping structures

In order to establish a first approximation of the relation between the locally absorbed radiation dose and the corresponding extinction coefficient, the idea is to irradiate a dosimetry gel with multiple beams that are spatially overlapping in some volume of the gel. In the case of two identical beams, the absorbed dose would then be twice as high as compared to regions where only one beam interacts with the gel and so on. Thus, by determining the local extinction coefficient and plotting its values as a function of the locally absorbed dose, one can obtain a relation between these two parameters. The two dosimetry gel samples intended for this purpose have irradiated structures according to Figure 6.18 where the simulated dose plans are depicted. The first dosimetry gel in panel (a) and panel (b) is irradiated with two beams that overlap in the center of the sample whereas the second cuvette in panel (c) and panel (d) is irradiated with one beam that is rotated  $360^\circ$  around the sample. As the samples are required to settle down for about 12 h after irradiation, the scan of the samples is implemented around 20 h later.

However, during the preparation process for the scan, i.e. positioning of the focus in the sample and determining an appropriate exposure time, both of the two new samples display a light sensitivity that had not been observed in the previously investigated samples. More precisely, the modulated laser sheet creates new layers in the form of planes in the samples that in turn strongly affect the light propagation and hampers any measurements on these samples. Figure 6.19(a) displays an image of the sample where several thin layers are clearly visible in the middle of the sample. In addition, Figure 6.19(b) displays the sample being irradiated with a laser in order to better visualize these planes. While the desired structures from the polymerization process induced by the irradiation can be described as milky-looking, the structures created by illumination with the laser sheet are rather blurry and strongly scatter the light, thereby destroying the modulation of the laser sheet which is vital for the approach employed here. In fact, the new structures look as if the laser light had melted the gel which then subsequent to the illumination, congealed again. There are different possible explanations on why the new

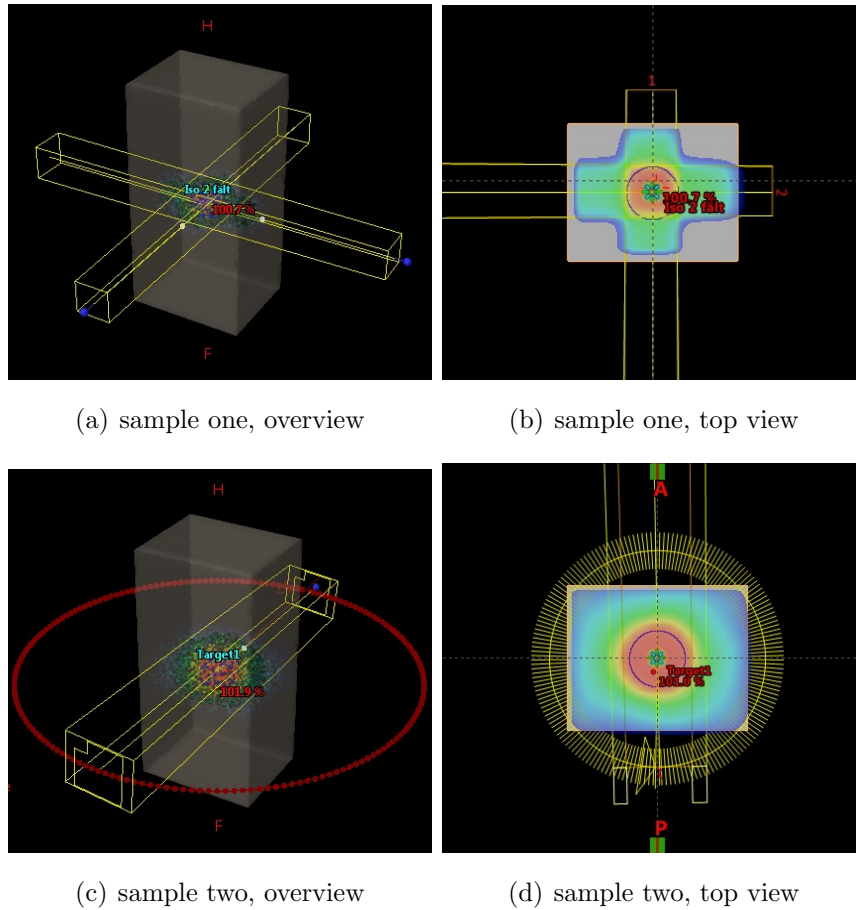


**Figure 6.18:** Simulated dose plan for the two samples under investigation. While the first sample in panels (a) and (b) is irradiated by two beams that overlap in the center of the gel, the second sample in panels (c) and (d) is irradiated by one beam that is rotated  $360^\circ$  around the sample. Images provided by Sofie Ceberg from the Division of Medical Radiation Physics at Lund University, Sweden.

samples exhibit the observed light sensitivity while the first dosimetry gels probed did not display any such behavior. As a first aspect, one may consider different concentrations of the constituents of the gel. Even though all gels probed as part of this thesis were created with the same recipe according to [16], mixing the gels is a manual process and small variations in concentrations are unavoidable and could maybe cause different light sensitivities of the gels. A further explanation might be that the 20 h time gap between the irradiation process and the scan is not sufficient in order for the samples to settle down. However, even several days after the irradiation process, the laser operating at full power still creates new structures in the samples. Moreover, one might consider the energy of photons which scales linearly with the inverse of the wavelength. As absorption and inelastic scatter processes in the gel cannot be completely ruled out, the involved energy transfers can lead to temperature increases that cause the gel to melt.

As a consequence, one can state that the results clearly demonstrate the necessity for

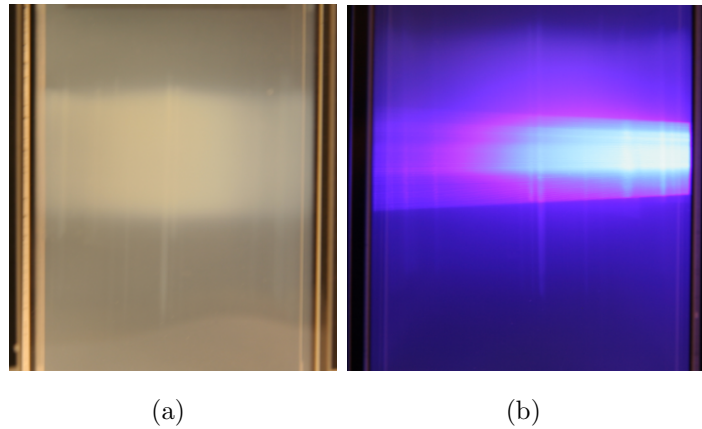


**Figure 6.19:** Illustration of the undesired planar structures in the dosimetry gel caused by illumination with the laser sheet. In panel (a), a plane is clearly visible in the middle of the image whereas in panel (b) where the gel is illuminated with a laser even more planes are visible.

further investigations concerning the light sensitivity of the dosimetry gels and possible means to avoid the observed effects which will also be discussed in Section 7. Due to the above described observations, establishing a relation between the extinction coefficient and the absorbed dose cannot be included as part of the work conducted here.

## 6.5 Limitations

Even though the new dosimetry technique investigated in this thesis is of great potential as shown in the previous sections, there are two limitations in applicability that were encountered during the project and will be addressed briefly in this section.

### 6.5.1 Scattering Particle Size

One aspect of importance for the applicability of the here presented technique is the size of the scattering particles in the probed sample. As the scattered light is detected at an angle of  $90^\circ$ , scattering should ideally be isotropic in order for the approach employed to extract the local extinction coefficient to be valid. In the case of non-isotropic scattering, a reduction in detected signal along the light propagation direction is not only caused by laser extinction but depends also on the scattering phase function and position of the scattering particle relative to the camera as illustrated in Figure 6.20(a). Here, the two scattering particles exhibit preferential forward scattering as indicated by the weight of the arrows. Assuming that the incident light on both particles is identical, the signal detected from the second scattering particle would be of lower intensity as none of the forward scattered light is detected from that particle. The probability for prefer-

ential forward scattering depends on the size of the scattering particle and increases for increasing particles according to [8]. In fact, when probing a homogeneous milk solution using whole milk with a fat content of 3.5 %, the resulting extinction coefficient displays the behavior illustrated in Figure 6.20(b). Despite using the exact same setup and algorithm as employed when probing the milk solutions in section 6.3 where milk with a fat content of 1.5 % was employed, one notices an increased extinction coefficient along the entrance side that decreases along the sample width as one moves further into the whole milk sample. From Figure 6.20(a) it follows that preferential forward scattering is a possible explanation for this behavior as it would lead to a stronger signal towards the entrance side of the laser sheet and thus, to higher extinction coefficients in this region. One distinct difference between whole milk and reduced fat milk is their particle size distribution. According to [17], most of the particles in whole milk have diameters in the range of  $0.4 \mu\text{m} - 2 \mu\text{m}$  whereas for low fat milk, particles of  $0.1 \mu\text{m}$  in diameter constitute the largest volume fraction. Keeping in mind that larger particles are more likely to exhibit preferential forward scattering, the difference in particle size distribution might very well be responsible for the increased extinction coefficient along the entrance side of the sample as observed in Figure 6.20.

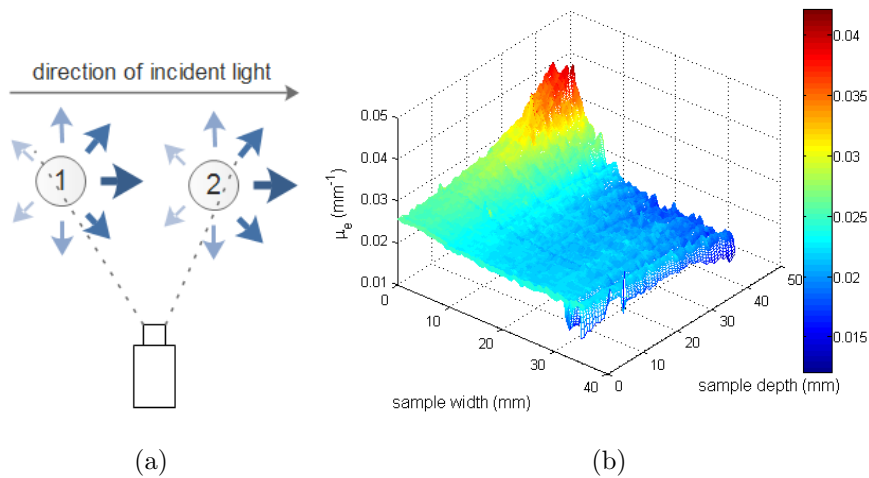


**Figure 6.20:** Panel (a) illustrates the influence of particle position relative to the camera in the case of preferential forward scattering. The calculated extinction coefficient for a homogeneous whole milk solution is depicted in panel (b) where one observes an increased  $\mu_e$  along the entrance side.

### 6.5.2 Limit in Optical Depth

As mentioned before, the approach employed here requires the modulation of the laser sheet to be visible in order to extract the SLIPI images. However, the longer the incident laser light and the generated signal travel through the sample, the more scattering inter-

actions occur and the line structure blurs out. In fact, when probing the homogeneous milk solution corresponding to the sample with highest milk concentration included in the linear fit (Section 6.3), one starts to notice a signal loss towards the exit side in the last layers of the sample. As higher milk concentrations correspond to a larger turbidity and stronger scattering, it is reasonable to assume that the optical depth in this region is too high for the modulation to remain detectable. Even though the position in the sample for which the signal loss starts appearing is difficult to determine as the transition is rather smooth, a value for the maximum optical depth  $OD_{max}$  that can be probed of around 3 is estimated.

However, it is important to note that this maximum optical depth that can be probed does not correspond to a fundamental limitation but is setup specific. For instance, by choosing a lower frequency for the intensity modulation of the laser sheet, one could increase the detectability of the line structure and thereby allow even samples of optical depths higher than  $OD_{max}$  to be probed. The reason for the high frequency modulation chosen for the work presented here is that the loss of spatial resolution when applying the SLIPI algorithm is proportional to the inverse of the modulation frequency as mentioned in Section 4.2. If one was to choose a lower frequency modulation, it is advisable to take three images according to Equation (4.9) instead of one single image as for the results presented here. Consequently, the time necessary to scan a sample would increase accordingly.



## 7 Summary and Outlook

The thesis work presented here investigated a novel approach to determine the locally absorbed radiation dose in a polymer gel used for dosimetric purposes in radiotherapy. Based on the side detection of light scattered by the sample, the local extinction coefficients were determined for the three-dimensional samples. The three major tasks addressed in this work were the experimental setup, the implementation of an algorithm to calculate the local extinction coefficient as well as the execution of first tests investigating the applicability of the new technique.

In order to allow a transport of the designed setup if necessary, all components were fit onto an optical base-plate of 40 cm x 70 cm. Using a combination of lenses, the output of a commercial laser at a wavelength of 447 nm was first compressed into a thin laser sheet with an approximate height of 4 cm. The laser sheet had a sinusoidal intensity variation along its height which was achieved by overlapping the two fundamental peaks of the interference pattern caused by a Ronchi grating in the beam path. Subsequently, the modulated laser sheet was directed into the dosimetry gel sample and scattered light was detected at an angle of  $90^\circ$  with a CCD camera. A technique referred to as Structured Laser Illumination Planar Imaging allowed the suppression of signal contribution from multiply scattered light, leading to an improved accuracy of results.

The calculation of the local extinction coefficient in the sample was implemented by assuming that laser extinction in the sample follows the Beer-Lambert law. More precisely, signal attenuation was considered to be negligible in the plane through the sample that is closest to the camera such that the extinction coefficient could be calculated from the difference in intensity between neighboring pixels in the light propagation direction for that specific plane. Moving the sample and thereby scanning the whole dosimetry gel slice-wise allowed the determination of the local extinction coefficient through the sample as the calculated local extinction coefficients for the preceding planes made it possible to include signal attenuation in the calculations. Using a software that automatically moved the sample and acquired the images, scanning the samples of length 4.5 cm with a step size of  $500 \mu\text{m}$  took only between 5 – 10 min depending on image acquisition time.

Verification of the results was achieved by probing homogeneous milk-water solutions. Considering the depth of field of the camera, reflection losses as well as camera position led to a constant extinction coefficient for the homogeneous solution which was interpreted as a quantitative verification. Moreover, a qualitative verification was obtained by plotting

## 7 Summary and Outlook

the extinction coefficient of milk solutions of different concentrations as a function of the concentration which resulted in a linear curve with only a small offset and data points that were in good agreement with a linear model.

Noticeable characteristics of the new approach are its independence of the absolute signal strength which was demonstrated using synthetic datasets, and its ability to visualize the irradiated structures in the sample as one could see when investigating a sample with irradiated pillar structure. However, the results also displayed some discrepancies to the expected behavior such as the increased extinction coefficient behind the pillar which cannot be neglected. For future investigations, it is therefore advisable to scan the sample twice with a  $180^\circ$  turn of the sample between the two scans. By doing so, one could take into account any shadow effects that structures in the sample might cause. In addition, the double-scan approach would also decrease the sensitivity of the new approach to polluting particles on the glass cuvettes. As was seen in the case of a homogeneous milk solution, polluting particles on the cuvettes can potentially block the signal from being detected and thereby result in the appearance of "ravines" in the determined extinction coefficient that pervade the entire sample. In the double-scan approach, this effect would be easy to detect and correct for as it is highly unlikely to find polluting particles at the exact same position on the front and back glasses of the cuvette. A further effect caused by polluting particles was observed within the sample. Here, the polluting particles caused extremely high signals originating from their location which led to an over-estimation of the local extinction coefficient in that point of the sample. It might therefore also be of interest to consider, for instance, the use of a median algorithm that scans the recorded signal for values that are unrealistically high as compared to the signal in neighboring pixels and corrects for any such behavior.

However, the most important next step is to investigate the light sensitivity of dosimetry gels as the structures created through illumination with a laser sheet made any measurement on samples irradiated by multiple beams impossible. If the structures are indeed caused by a raise in temperature that locally melts the gel as a result of energy transfers between the photons and the gel, a change of laser wavelength to larger values could maybe help as photons of longer wavelengths are less energetic. Once the cause of these structures has been identified and corrected for, one can establish a relation between the experimentally determined local extinction coefficient and the absorbed dose which is vital for the pursued dosimetric applications. If samples of optical depths greater than an optical depth of 3 are to be probed for these measurements, one would have to also lower the modulation frequency in order for the modulation to remain detectable. On top of that, an uncertainty estimation of the results is necessary for which probing a sample of well known extinction coefficient would be helpful.

All in all, the work presented here has led to a complete setup with which the signal of interest can be be acquired as well as the algorithm necessary for calculating the lo-

cal extinction coefficient of the sample. Despite having encountered various effects such as reflections or vignetting that strongly influenced the results, a quantitative as well quantitative first verification of result was achieved by implementing means to account experimentally or compensate numerically for these influences. Even though further investigations are necessary to explain certain observed discrepancies between the results and theoretical expectations, the outcome of the work presented here clearly shows a strong potential of the new technique as it allows the irradiated structures to be visualized with high resolution.



## 8 Bibliography

- [1] B. W. Stewart and C. P. Wild, editors. *World Cancer Report 2014*. International Agency for Research on Cancer, 2014.
- [2] Cancer Research UK. What radiotherapy is. <http://www.cancerresearchuk.org/about-cancer/cancers-in-general/treatment/radiotherapy/about/what-radiotherapy-is>, data retrieved on May 2nd 2015.
- [3] S. Ceberg. *3D Verification of Dynamic and Breathing Adapted Radiotherapy using Polymer Gel Dosimetry*. Medical radiation physics, Department of Clinical Sciences (Malmö), Lund University, Skane University Hospital, 2010.
- [4] M. J. Maryanski, J. C. Gore, R. P. Kennan, and R. J. Schulz. Nmr relaxation enhancement in gels polymerized and cross-linked by ionizing radiation: a new approach to 3d dosimetry by mri. *Magn Reson Imaging*, 11:253–8, 1993.
- [5] E. Berrocal, E. Kristensson, M. Richter, M. Linne, and M. Aldén. Application of structured illumination for multiple scatterin suppression on planar laser imaging of dense sprays. *Optical Society of America*, 16(22), 2008.
- [6] E. Kristensson. *Structured Laser Illumination Planar Imaging (SLIPI) - Applications for spray diagnostics*. PhD thesis, Division of Combustion Physics, Department of Physics, Lund University, 2012.
- [7] R. Wellander, E. Berrocal, E. Kristensson, M. Richter, and M. Aldén. Three-dimensional measurement of the local extinction coefficient in a dense spray. *Measurement Science and Technology*, 22, 2011.
- [8] C. Bohren and D. Huffman. *Absorption and Scattering of Light by Small Particles*. Wiley-VCH, 1983.
- [9] C. Baldock, Y. D. Deene, S. Doran, G. Ibbott, A. Jirasek, M. Lepage, K. B. McAuley, M. Oldham, and L. Schreiner. Polymer gel dosimetry. *Physics in Medicine and Biology*, 55(5):R1–63, 2010.
- [10] A. Fuxman, K. B. McAulMc, and L. J. Schreiner. Mdosimetry free-radical crosslinking copolymerization of acrylamide and n,n'-methylenebis(acrylamide) for radiation dosimetry. *Macromolecular Theory and Simulations*, 12(647-662), 2003.

## 8 Bibliography

- [11] Y. De Deene, K. Vergote, C. Claeys, and C. De Wagter. The fundamental radiation properties of normoxic polymer gel dosimeters: A comparison between a methacrylic acid based gel and acrylamide based gels. *Phys. Med. Biol.*, 51(3):653–73, 2006.
- [12] P. J. Keall and C. Baldock. A theoretical study of the radiological properties and water equivalence of three types of gels used for radiation dosimetry. *Australas Phys Enf Sci Med*, 1999.
- [13] L. E. Olsson, S. A. J. Bäck, P. Magnusson, and P. Haraldsson. 3d dosimetry using gels and mri in imaging in radiatio therapy. *AAPM Monograph*, (24), 1998.
- [14] E. Kristensson, J. Bood, M. Alden, E. Norsström, j. Zhu, S. Huldt, P.-E. Bengtsson, H. Nilsson, E. Berrocal, and A. Ehn. Stray light suppression in spectroscopy using periodic shadowing. *Optics Express*, 22(7), 2014.
- [15] B. E. A. Saleh and M. C. Teich. *Fundamental of Photonics*. John Wiley & Sons, Inc. Wiley Series in Pure and Applied Optics, second edition edition, 2007.
- [16] Sofie Ceberg. This information was obtained in a conversation with Sofie Ceberg who provided the samples investigated in this thesis.
- [17] Beckman Coulter. *Milk fat size distribution by laser diffraction*. [https://www.beckmancoulter.com/wsrportal/bibliography?docname=BCPCS002\\_LE.pdf](https://www.beckmancoulter.com/wsrportal/bibliography?docname=BCPCS002_LE.pdf), data retrieved on May 15th 2015.

# Acknowledgments

**Elias Kristensson:** Thank you for your willingness to guide me throughout the entire process. Your illustrative explanations and examples always helped me to understand concepts better and your approachability has made working with you a very enjoyable experience. Not to mention, you have been an inspiration to me as a researcher and I learned incredibly much from you.

**Edouard Berrocal:** Every time we met, you had uncountable ideas concerning my project and it was an inspiration discussing those with you.

**Sophie Ceberg & Sven Bäck:** Thank you for providing the samples I investigated in this thesis and for answering all my dosimetry-related questions.

**Deborah Guo:** Even though this past year has been tedious, you always had my back and supported my efforts by thoroughly proof-reading every single of submitted reports. I could not have done it without you.

**Family:** I would like to thank all of you; my parents, Angelika and Detlef, my sister, Lisa, and my grandma, Dorothea Hocke, for your love and support. I would have never made it here without you.